2021-02-10

An Evaluation of the Constant Flux Layer in the Atmospheric Flow above the Wavy Air-Sea Interface

Ortiz-Suslow, David G.; Kalogiros, John; Yamaguchi, Ryan; Wang, Qing

AGU

An Evaluation of the Constant Flux Layer in the Atmospheric Flow above the Wavy Air-Sea Interface

David G. Ortiz-Suslow[1], John Kalogiros[2], Ryan Yamaguchi[1], and Qing Wang[1]

[1]Department of Meteorology, Naval Postgraduate School, Monterey, CA
[2]National Observatory of Athens, Athens, GR

Key Points:

- Profiles of eddy covariance fluxes were used to evaluate the prevalence of the constant flux layer in the air above the ocean.
- Only 1/3 of momentum flux gradients were satisfactorily constant; prevalence tended to be substantially higher for the heat fluxes.
- Flux divergence was strongly linked with turbulence non-stationarity, swell-wind alignment, and moderate-strong stability conditions.

Corresponding author: D. G. Ortiz-Suslow, `dortizsu@nps.edu`

This article has been accepted for publication and undergone full peer review but has not been through the copyediting, typesetting, pagination and proofreading process, which may lead to differences between this version and the Version of Record. Please cite this article as doi: 10.1029/2020JD032834.

Abstract

The constant flux layer assumption simplifies the problem of atmospheric surface layer (ASL) dynamics and is an underlying assumption of Monin-Obukhov Similarity Theory, which is ubiquitously applied to model interfacial exchange and atmospheric turbulence. Within the marine environment, the measurements necessary to confirm the local ASL as a constant flux layer are rarely available, namely: direct observations of the near-surface flux gradients. Recently, the Research Platform *FLIP* was deployed with a meteorological mast that resolved the momentum and heat flux gradients from 3 to 16 m above the ocean surface. Here, we present findings of a study assessing the prevalence of the constant flux layer within the ASL, using an approach that accounts for wave-coherent turbulence, defines the wave boundary layer height, and empirically quantifies the observed flux divergence. Our analysis revealed that only 30-40% of momentum flux gradients were approximately constant; for the heat fluxes, this increased to 50-60%. The stationarity of local turbulence was critical to the constant flux layer's validity, but resulted in excising a large proportion of the observed profiles. Swell-wind alignment was associated with momentum flux profile divergence under moderate wind speeds. In conjunction, our findings suggest that the constant flux layer, as it is conventionally defined, is not generally valid within the marine ASL. This holds significant implications for measuring air-sea fluxes from single point sources and the application of Monin-Obukhov similarity theory over the ocean.

Plain Language Summary

Our ability to quantify the exchange of energy and material (e.g., gas) between the atmosphere and ocean has greatly improved over the second half twentieth and into the beginning of the twenty-first centuries. While there have been significant technological and methodological advancements within the community of researchers studying this problem, a central theory to the physical framework we use to conduct the majority of studies has not been adequately validated or assessed using observations over the ocean. The constant flux layer model (or assumption) greatly simplifies the physical problem of studying the atmosphere near the ocean surface, but the data necessary to validate this theory are rarely collected. A recent field campaign deployed a unique ocean-going platform that enabled us to conduct this much needed evaluation. We found strong evidence suggesting that the constant flux layer model is only valid within the general marine environment at most 50-60% of the time. We also found that the prevalence of this theory's validity differed between the exchange (i.e., flux) of kinetic energy and heat, two critical parameters controlling the atmosphere-ocean system. Our findings suggest that the simplified physics we rely on to study air-sea exchange needs to be critically re-evaluated.

1 Introduction

The airflow within the marine atmospheric surface layer (MASL) directly interacts with the underlying ocean. Unlike over land, the complexity of this four-dimensionally varying, turbulent flow is enhanced by the presence of a dynamic surface. With the advance of high resolution numerical modeling and forecast systems, there is a more urgent need to better quantify the mean and turbulent structure of the MASL and how this impacts atmospheric processes and air-sea interaction in all conditions. In particular, it is being recognized that the work of the previous century helped develop a general understanding of MASL dynamics, that nonetheless over-simplified the physics, which must be better understood.

The overwhelming majority of previous MASL field datasets relied on point measurements of atmospheric mean and flux parameters deployed from ships, buoys, and/or other platforms. Broadly speaking, the primary aim in collecting these data was to develop bulk parameterizations of the surface fluxes of momentum, sensible and latent heat

(Fairall, Bradley, Rogers, Edson, & Young 1996; W. Large & Pond 1981; W. G. Large & Pond 1982; Smith 1980, 1988; Smith & Banke 1975; Wu 1982; Yelland & Taylor 1996). This effort largely focused on developing empirical relationships between the bulk exchange coefficients: C_D, C_T, and C_E (the aerodynamic drag, Stanton, and Dalton coefficients, respectively) and mean environmental forcing, e.g. wind speed and/or surface gravity waves (Andreas, Mahrt, & Vickers 2014; Charnock 1955; Donelan et al. 2004; J. B. Edson et al. 2013; Högström et al. 2018; Jeong, Haus, & Donelan 2012; Kitaigorodskii & Volkov 1965; Powell, Vickery, & Reinhold 2003).

In order to quantify the air-sea exchange from a single flux measurement made at an altitude z within the MASL, investigators must assume their fluxes are equivalent to the values at the top of the wave boundary layer (WBL), because this is the flux that physically drives interfacial exchange. This assumption presumes the MASL is a constant flux layer, a classic fluid mechanics concept applied to wall-bounded shear flows. Whether or not a measurement is made within this layer directly impacts the applicability of Monin-Obukhov Similarity Theory (MOST), which is ubiquitously applied to studying or modeling the MASL using the well-known flux-gradient relationships (J. B. Edson & Fairall 1998). Following MOST, the flux-gradient relationship for X takes the form:

$$\frac{\partial X}{\partial z}\frac{z}{x_*} = \phi(\zeta), \tag{1}$$

where x_* is the turbulent scale for X and ζ is the stability parameter, z/L, with L being the Obukhov length. In the cause of neutral stability, $\phi \rightarrow 1$ (for momentum) and the familiar logarithmic profile is recovered. Conventionally, ϕ (and its integrated form ψ) is defined (Businger, Izumi, Bradley, & Wyngaard 1971) assuming x_* is a constant over the entire integrated profile, usually taken as the span of z_0 (the roughness length scale for X) to the altitude of the measurement z or some other reference (e.g., 10 m). While a significant amount of effort has been expended in addressing various aspects of data quality control and assessment, such as platform motion and tilt corrections (Anctil, Donelan, Drennan, & Graber 1994; J. B. Edson et al. 1998; Wilczak, Oncley, & Stage 2000), the critical assumption that $x_* \neq f(z)$ remains largely untested for most MASL datasets. Therefore, investigators must rely on the widespread validity of the constant flux layer assumption, which may be doubtful from both an experimental (Wyngaard 1990) and theoretical basis (Tennekes 1973).

Over the ocean, detailed profile measurements remain rare because of the significant challenges to deploying a vertically-distributed sensor array capable of making robust turbulence measurements within the MASL. The Research Platform *FLIP* remains an ideal ocean-going platform specifically designed for this purpose (Miller, Hristov, Edson, & Friehe 2008). Since its commission (Fisher & Spiess 1963), *FLIP* has been deployed for several air-sea interaction campaigns where multiple levels of atmospheric variables were measured, such as during SCOPE (Fairall, Bradley, Hare, Grachev, & Edson 2003), the MBL/ARI experiment (Miller, Friehe, Hristov, Edson, & Wetzel 1999), COPE (Grachev, Fairall, Hare, Edson, & Miller 2003), and HiRes (Grare, Lenain, & Melville 2013). At shorelines (recently, Fang et al. 2018; Katz & Zhu 2017; Shabani, Nielsen, & Baldock 2014; Zhao et al. 2015) or inland waters (Li, Bou-Zeid, Vercauteren, & Parlange 2018), towers have been deployed with turbulence profiles and some assessment of the gradients were conducted. However, these evaluations were limited in scope and tended to assume that the flux variance was randomly distributed, as in a mean ± standard deviation adequately flagged divergent flux gradients. Furthermore, profiles tended to be limited in their number of observing levels, <4 for Fang et al. (2018); Katz and Zhu (2017); Li et al. (2018); Shabani et al. (2014); Zhao et al. (2015), and due to their proximity to the land-sea boundary are not representative of the open ocean.

Recently, Mahrt, Miller, Hristov, and Edson (2018) used previously collected field data to re-visit analysis of the wind stress and address some issues regarding stress divergence. Among the datasets used in that study were measurements from *FLIP* during RED (Högström et al. 2013) and MBL (J. B. Edson et al. 1998), as well as the coastal measurements from the Martha's Vineyard coastal observatory during CBLAST (J. Edson et al. 2007) and from the Östergansholm tower in Sweden (Hogstrom et al. 2008). In this study, they identify that substantial stress divergence is quite common within the MASL and they assume a linear gradient in the observed momentum flux to devise the corresponding surface stress from the observed stress. From this, they estimated the depth of momentum flux divergence to be on average 49 m, with extrema 23 and 75 m from the CBLAST and Östergansholm (only the case of weak cross-swell winds), respectively (see their Table 1). This work helps address some of the uncertainty surrounding the validity of the constant flux layer assumption over the ocean, but their analysis was somewhat limited by the diversity in data collection techniques and measured quantities within these disparate field studies and their focus was on the momentum flux.

Here we present an experimental analysis of the complete flux profile (momentum and total heat) within the MASL over the course of the Coupled Air Sea Processes and Electromagnetic ducting Research (CASPER) west coast field campaign. CASPER-West was a large-scale, comprehensive air-sea interaction study aimed at understanding the impact marine atmospheric boundary layer (MABL) variance has on electromagnetic (EM) and electro-optical (EO) propagation above the ocean surface (Wang et al. 2018). To the authors' knowledge, the present study is one of the first observation-based, systematic evaluations of the constant flux layer assumption over the ocean that considers the flux gradients of momentum, temperature, and water. The aim of this study is not to determine the physical mechanism driving stress divergence. Rather, the goal is to assess the statistical prevalence of the constant flux layer, using the *FLIP* data as a test case approximating deep ocean conditions. One of our central aims in conducting this analysis was to determine the environmental conditions for which MOST can be applied within the MASL. The findings of our work provide guidance on the experimental design of near-surface observation campaigns, MASL data interpretation and modeling.

2 Theoretical Basis for the constant flux Layer Model within the Atmospheric Surface Layer

There are two facets to understanding the constant flux layer model within the atmospheric surface layer (ASL): (1) it's theoretical foundation and (2) how this applies within the context of the atmospheric boundary layer governing equations. The former focuses on how this model arises from an idealized, wall-bounded shear flow and the latter provides insight into our expectations for the flux gradient within an idealized boundary layer.

2.1 An Ideal Origin

Fundamentally, the origin for a constant flux layer stems from Prandtl's mixing length model as applied to the turbulence of a wall-bounded shear flow. The derivation of the constant flux layer model is a classical fluid mechanics exercise that can be found in many reference texts, the source for much of the review presented here is Tennekes and Lumley (1972) (see chapter 2.5). This brief, and somewhat pedantic, review is relevant to the atmospheric problem, but not directly applicable to the MASL given the idealized setup and that it does not account for the wavy interface (c.f., Kraus & Businger 1994).

We will consider a two-dimensional $x-z$ (x is stream-wise and z is vertical) plane, with a steady, barotropic mean flow. U is the mean, stream-wise flow speed, which only varies with z. For our purposes, we will allow the wall to be porous such that there is a constant mean W ($\frac{\partial W}{\partial x} = \frac{\partial W}{\partial z} = 0$). This trans-interfacial velocity can be a blowing or suction velocity and the purpose of including this at all is discussed below. In this scenario, the Reynolds Averaged Navier-Stokes (RANS) equations are greatly simplified and the stream-wise equation takes the form,

$$W\frac{\partial U}{\partial z} = \frac{1}{\rho}\frac{\partial \tau_{xz}}{\partial z}. \tag{2}$$

Integrating this equation yields,

$$\rho\, w_m\, U = \tau_{xz} - \tau_0, \tag{3}$$

where τ_0 is the Reynolds stress at the surface ($z = 0$). Assuming a no slip boundary ($U_{z=0} = 0$), $\tau_0 \equiv \rho\, u_*^2$. Here, we have defined $W \equiv w_m$, which we will term the transfer velocity from between the wall and flow. τ_{xz} is the total mean stress, but without a mean pressure gradient and outside of the viscous sublayer ($zU/\nu >> 1$), viscosity's (ν) impact on the shear stress can be neglected and eqn. (3) can be written as:

$$w_m U = -\overline{w'u'} - u_*^2, \tag{4}$$

where $-\overline{w'u'}$ is the along-stream Reynolds stress (the covariance between the stream-wise, u', and vertical, w', perturbation velocities), also referred to as the vertical flux of horizontal momentum. This is a localized quantity, which *can* vary with z.

In the case of $w_m = 0$ (assuming a solid wall), eqn. (4) states that $u_*^2 \equiv \overline{w'u'}$, implying that over some span-wise distance near the wall, but outside the viscous sublayer, the local Reynolds stress (i.e. vertical flux of horizontal momentum) is equivalent to the shear stress at the wall. Therefore, the kinematics within this inertial-sublayer are governed by a *single* turbulent velocity scale (u_*) and one relevant length scale, z. For atmospheric surface layer flows, this has the practical significance of simplifying the task of quantifying the surface wind stress ($\tau_{wind} = \tau_0 = \tau$) and modeling the dissipation of turbulence kinetic energy (Batchelor 1947; Kolmogorov 1941a, 1941b).

We could have arrived at this same conclusion directly from eqn. (2), if we had assumed that $W = 0$ from the start, such that $\partial\tau_{xz}/\partial z = 0$, i.e, a non-divergent stress gradient. However, it was instructive to use w_m to emphasize that the constant flux layer model *only* arises when there is one relevant turbulent scale. Herein, the phrases "constant flux layer" and "non-divergent stress" or "flux" will be used interchangeably, as well as the converse (e.g., divergent stress signifies there is a flux gradient which means we cannot assume the presence of a constant flux layer).

2.2 The Constant Flux Layer within the Idealized Atmospheric Boundary Layer

The horizontal momentum balance equations for the idealized atmospheric boundary layer take the form,

$$\rho\left(\frac{\partial U}{\partial t} + U\frac{\partial U}{\partial x} + V\frac{\partial U}{\partial y}\right) = -fV + \frac{\partial}{\partial x}\left[-P + 2\mu\left(\frac{\partial U}{\partial x} + \frac{\partial U}{\partial y}\right)\right] + \rho\frac{\partial}{\partial z}(-\overline{w'u'}), \tag{5}$$

$$\rho\left(\frac{\partial V}{\partial t} + U\frac{\partial V}{\partial x} + V\frac{\partial V}{\partial y}\right) = +fU + \frac{\partial}{\partial y}\left[-P + 2\mu\left(\frac{\partial V}{\partial x} + \frac{\partial V}{\partial y}\right)\right] + \rho\frac{\partial}{\partial z}(-\overline{w'v'}), \tag{6}$$

where f is the Coriolis frequency ($2\Omega\, sin\theta$), P is the hydrostatic pressure, the $2\mu()$ terms are the mean strain rate, and the last term on the r.h.s. is the relevant Reynolds stress. As is often done, these equations are further simplified by assuming stationary, homogeneous conditions outside of the viscous sublayer; and using the limit of geostrophic wind balance (see §9.6 Wyngaard 2010), one can show these reduce to(Blackadar & Tennekes 1968):

$$-f(V - V_g) = \frac{\partial}{\partial z}(-\overline{w'u'}) \tag{7}$$

$$f(U - U_g) = \frac{\partial}{\partial z}(-\overline{w'v'}), \tag{8}$$

where g denotes the geostrophic wind component ($-fU_g = \frac{1}{\rho}\partial P/\partial x$). Assuming first order asymptotic solutions in the region of the boundary layer termed the inertial sub-layer, integrating eqns. 7-8 yields the following dimensionless relationships (Tennekes 1973):

$$-\frac{\overline{w'u'}}{u_*^2} = 1 - \frac{A\,f\,z}{\kappa\,u_*} \tag{9}$$

$$-\frac{\overline{w'v'}}{u_*^2} = \frac{f\,z}{\kappa\,u_*} log\left(\frac{f\,z}{u_*}\right), \tag{10}$$

where $A = 5$ and κ is the Von Kármán constant (here, taken as 0.41). Using $f \approx 1.45 \times 10^{-4}$, one can generate representative profiles of the theoretically expected Reynolds stress gradient (Figure 1). This exercise was done using the actual altitudes of the *FLIP* meteorological mast during CASPER-West (see below). These profiles reveal that for very low wind forcing, $u_* \sim 0.03$ ms^{-1}, the local stress decreases from 0.8 to 0.5 of the surface value from $z = 3$ to 16 m, respectively. However, for $u_* \sim 0.1$ (corresponding to approximately $U = 3$ ms^{-1}), the the local stresses across 3-16 m are within 25% of the surface value and only vary internally by 20%. Experminetally, the observed, local stress is derived from the local friction velocity:

$$u_{*z}^2 = \sqrt{(-\overline{w'u'})^2 + (-\overline{w'v'})^2}. \tag{11}$$

It is important to note that the profiles in Fig. 1 assume a neutral atmosphere and do not account for surface gravity waves. Also, apart from the cases where $u_* \to 0$, the theoretical stress gradients vary linearly with z (Figure 1).

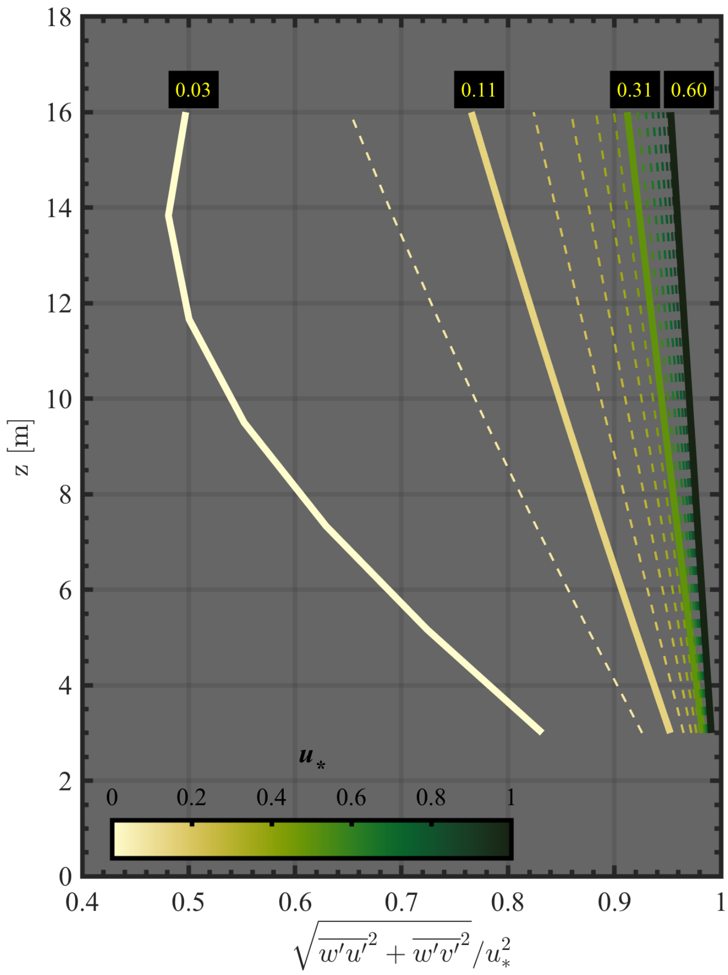

Figure 1. Idealized profiles reflecting the magnitude of eqns. 9 and 10 calculated over the actual altitude range of the CASPER-West *FLIP* mast. 15 cases of u_*, ranging sequentially (left-to-right) from 0.03 to 0.6 ms^{-1}, were tested, the corresponding u_* of the thick curves are noted.

As Tennekes (1973) discusses, equations 9-11 would suggest that the (M)ASL can *never* be considered a constant flux layer, thus precluding the premise of this study. However, in practice, it is generally assumed that, over some finite altitude (z) within the total boundary layer height (H), the flux is *effectively* constant. Wyngaard (2010) argues that the mean, along-stream Reynolds stress gradient should scale as,

$$\frac{u_*^2}{H} \sim \frac{\partial \overline{w'u'}}{\partial z}, \tag{12}$$

and must be very small (<< 1) if non-dimensionalized,

$$\frac{z}{u_*^2}\frac{\partial \overline{w'u'}}{\partial z} \sim \frac{z}{H}, \tag{13}$$

which is typically the case for measurements made within the surface layer ($z \leq 10$ m) with a boundary layer height $H = 500 - 1000$ m. Wyngaard's scaling argument provides a rationale for neglecting the vertical stress gradient and is supported by the gradients in Figure 1, which quickly converge to unity as the wind stress approaches typical MASL conditions.

Under ideal circumstances, marine platform-based ultrasonic anemometry and eddy covariance techniques yield a maximum precision of approximately ±10%, i.e., the error in a single estimate of u_{*z} (J. B. Edson et al. 1998; Wyngaard 1990). Of course, the actual precision varies depending on the experimental factors and the amount of uncertainty investigators are willing to accept is an idiosyncratic threshold. However, if we rely on 10% as a rule-of-thumb, then two independent stress measurements separated by Δz, can differ by as much as 20% and be considered effectively equivalent. For typical field campaigns, Δz will be a few to at most 10 m for successive flux levels, over the ocean Δz tends to be much smaller because of practical considerations. This ~20% criteria coincides with eqns. 9-10 under low-moderate wind speeds and near-neutral conditions.

3 Methodology and Approach

3.1 Field Data

CASPER-West was a large scale field campaign aimed at characterizing the marine atmospheric boundary layer (MABL) variability along an approximately 50 km line from Pt. Mugu across the Santa Monica Basin south-southeast of Pilgrim Banks. For this study, the primary focus will be on the atmospheric measurements made from *FLIP*, which is a quinquagenarian,108 m floating platform that is specifically designed (Fisher & Spiess 1963) to minimize its direct response to surface gravity waves. Thus, *FLIP* is an ideal platform for making robust, near-surface measurements on both sides of the air-sea interface in a range of environmental conditions. For CASPER-West, *FLIP* was moored within the Southern California Bight, along the southern slope of the Santa Monica Basin, from September 22 to October 25, 2017.

On the port-side boom of *FLIP*, a 13 m mast was deployed and outfitted with overlapping profiles of bulk and turbulence-resolving atmospheric measurements that captured MASL properties from approximately 3-16 m above the ocean surface. Herein the turbulence-resolving profile will be referred to as the *flux* profile and *bulk* will be used to refer to parameters observed by slow-response sensors where the primary variable of interest is the time average (e.g., wind speed, air temperature, and humidity). For the bulk profile, the wind vector $\mathbf{U}$ was measured using 10 Vaisala WMT/WXT (5 of each) two-dimensional sonic anemometers over a span of 5-15.9 m. The bulk profiles of temperature (θ) and humidity (q) were acquired using a total of 15 Rotronic (4 units, HC2A-S3) and Vaisala (11 units, HMP 155) probes spanning from 5.02-16.2 m above the surface. All of the bulk data were sampled at 0.5 Hz. For the flux levels, the lowest to highest were: RM Young (20 Hz sampling), Campbell Scientific CSAT-3 combined with a LI-COR LI-7500 gas analyzer (20 Hz sampling), and five Campbell Scientific IRGASON systems (50 Hz sampling). These seven flux systems were distribute quasi-logarithmically from 3-16 m above the mean water level.

Post-experiment, a thorough data quality investigation was conducted on both the bulk and flux datasets, the details regarding this analysis are summarized in a technical report (Ortiz-Suslow et al. 2019). Most relevant to this study, the lowest and uppermost fast-sampling hygrometer data were deemed too poor to include in these data, most likely due to contaminations on the glass—the mast was deployed in a such a way as to preclude routine cleaning. Therefore, for the water vapor flux profiles, only five levels will be analyzed. Also, a wind sector was determined where the observed turbulence was free from significant flow distortions from the superstructure and mounting apparatus (see report for details). For all of the analysis here, an averaging window of 30 minutes was used with successive window overlap being 50%.

3.2 Wave-Coherent Turbulence Filtering and Defining the Interface Between the Wave Boundary and Atmospheric Surface Layers

In the turbulent air flow immediately above the ocean surface waves, the total wind vector, $\mathsf{u} \equiv (\mathsf{u}, \mathsf{v}, \mathsf{w})$, is comprised of three components, $\mathsf{u} = \mathbf{U} + \mathbf{u}' + \tilde{\mathbf{u}}$. Here, the components u, v, and w are the along-, across-, and vertical-wind components, respectively; a capital indicates the average or bulk quantity derived over some averaging window ($\bar{~}$), primes indicate the Reynolds turbulence component ($\overline{u'} \equiv 0$), and for this study, the dispersive stress component ($\tilde{~}$) was attributed solely to wave-induced fluctuations. This last component is unique to the flow within the MASL, which interacts with a dynamic surface, unlike the classical wall-bounded shear flow scenarios or the terrestrial surface layer. The wave-induced signal can be buried within any turbulent record above the ocean.

Over the past few decades, the impact this wave-coherent contribution can have on the turbulence (co-)spectrum has been reported from observations (Högström et al. 2015; Rieder & Smith 1994) and it is no longer sufficient to assume that $\tilde{\mathbf{u}} = 0$ within the MASL—especially within a few meters of the surface. The wave-coherent turbulent stress ($\tilde{\tau} = \rho\overline{\tilde{w}\tilde{u}}$) begins to dominate the total (τ) stress near the interface within the wave boundary layer (WBL) (D. V. Chalikov & Makin 1991; Janssen 1989). While the importance of accounting for the wave-coherent airflow widely recognized, there appears to be discord in how the WBL is literally defined and applied.

On the one hand, it is theoretically expected that $\overline{\tilde{w}\tilde{u}}/\mathsf{u}_*$ decays exponentially with altitude and reaches zero very quickly from the surface—within at most a couple times the significant wave height, H_s (D. Chalikov 1995; D. V. Chalikov & Makin 1991). This is supported by tower measurements (Wetzel 1996) and field studies (e.g. Cifuentes-Lorenzen, Edson, & Zappa 2018; Potter et al. 2015) have used this profile to define the WBL depth, z_{wbl}. Using an idealized model framework, D. V. Chalikov and Makin (1991) proposes that $\overline{\tilde{w}\tilde{u}}$ becomes negligible at approximately $0.022\omega_p^{-1.66}$, where ($_p$ indicates at the surface wave spectral peak, ω is angular wave frequency, and g is gravitational acceleration). For the entire CASPER-West data, the mean height where $\overline{\tilde{w}\tilde{u}} \approx 0$ is 2.03±0.96, which agrees with the Cifuentes-Lorenzen et al. (2018) estimates of 1-3 m from the southern ocean. However, D. Chalikov (1995) provides a complete definition:

> The wave boundary layer (WBL) is the lower part of the atmospheric boundary layer above the sea, whose structure is influenced directly by the surface waves. Within the WBL, some portion of momentum transfer results from wave-produced fluctuations of pressure, velocity, and stresses....Moreover, the main dynamic atmosphere-ocean interaction takes place in the lowest part of the WBL within a height of about H_s,

which is at odds with the definition applied in the field studies highlighted above. According to the theoretical framework developed by Chalikov (and colleagues), who has remained focused on this problem over several decades (D. Chalikov 1995; D. Chalikov & Rainchik 2011; D. V. Chalikov 1978; D. V. Chalikov & Makin 1991), the height at which $\overline{\tilde{w}\tilde{u}} \approx 0$ is not the total depth of the WBL, rather it is an important sublayer. The *total* WBL depth should be of order the peak wavenumber, $k_p^{-1} = g\omega_p^{-2}$; for CASPER-West, the mean WBL height was estimated as 11.0±6.3. This altitude is more in-line with some previously reported tower- and *FLIP*-based turbulence profile measurements (Grachev & Fairall 2001; Grare et al. 2013; Smedman et al. 1999). These studies were not necessarily concerned with defining a WBL height, but rather reported the extent at which direct wave-coherent airflow was observed.

Apparently, there are inconsistencies in the literature on how the WBL is defined and applied. For the purposes of this study, we will define the WBL as the portion of the MASL where wave-coherent motion comprises a substantial portion of the total turbulent kinetic energy. This aligns more with Chalikov's definition because the peak wave length is more relevant than the wave height for the vertical extent of these motions. We expect that the vertical velocity, w, responds most directly to the surface wave motion and therefore is the physically appropriate parameter to use to diagnose the vertical extent of the WBL (in fact, pressure would be the *most* relevant parameter, but this was not measured adequately during CASPER-West). As part of our method for finding z_{wbl}, we used an empirical wave form filter to decompose the wave-coherent and Reynolds turbulence components of u. Hristov, Friehe, and Miller (1998) presented a method to remove the wave-coherent component of a turbulence record using the discrete Hilbert transform (Kak 1970). This Hilbert-Hristov filter (HHF) utilizes a wave response signal to construct a carrier wave time series that can be negated from the observed turbulence, $\mathbf{u_f} \equiv \mathsf{u} - \tilde{\mathbf{u}}$. For this study, the HHF was applied to the velocity, temperature, and water vapor using the laser altimeter record (50 Hz) installed on *FLIP*'s port boom to recover the wave signal.

In order to approximate z_{wbl} for each profile, the ratio of the filtered and observed vertical velocity variance, $\sigma^2_{w_f}/\sigma^2_{\mathsf{w}}$, was searched for the first measurement level exceeding the limit 0.8. Thus, z_{wbl} defines the altitude of the WBL-ASL interface. In the case of an entire profile $\sigma^2_{w_f}/\sigma^2_{\mathsf{w}} < 0.8$, then it was assumed that the entire *FLIP* mast was within the WBL and the ASL could *not* be defined. In the case, of the lowest level in the profile > 0.8, then it was assumed that the entire mast was within the ASL and a WBL could *not* be defined. Cases where only one measurement level was in the ASL (or WBL), were grouped with the appropriate null case. Figure 2 provides the distribution of the defined z_{wbl}. The measurement altitudes were not interpolated, therefore the "true" WBL height might actually be in between two levels. z_{wbl} shifts lower under stationary conditions (see Section 3.4) and was bi-modal. Under stationary conditions, there are as many cases (20-30%) with $z_{wbl} \approx 3$ m, as there are cases with $z_{wbl} \approx 16$ m. This largely reflects the fact that during CASPER-West (a) there was a strong diurnal wind and windsea, and (b) there was always background swell that dominated the wave field when the wind was very low during local mid-day.

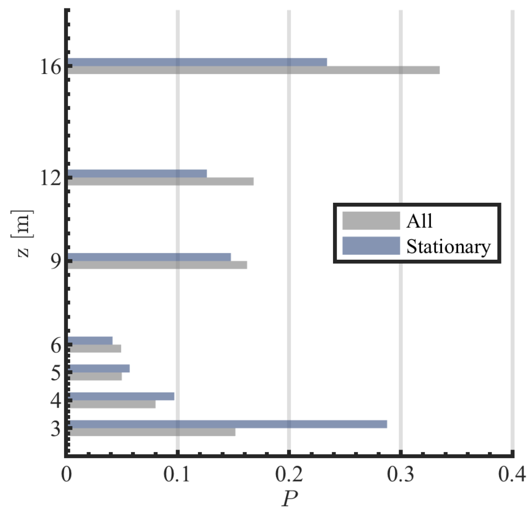

Figure 2. The probability (P) of determining the WBL at a particular measurement altitude z for all observations (gray) and those under purely stationary conditions (blue; see Section 3.4).

3.3 Definition of Surface Wave Spectral Energy Bands

A Datawell directional waverider buoy (CDIP #234) was moored within 1 km of *FLIP*'s location and the data from this platform was used to compare the turbulence profile to the underlying sea state. During CASPER-West, the sea state was persistently mixed, with three directionally-distinct energy bands identifiable throughout much of the experiment: E_s, E_m, and E_w, where E is the surface elevation variance density and subscripts represent the low frequency swell (s), mid-frequency swell (m), and local wind-sea bands (w), respectively. The three bands were separated by f_s (an arbitrary limit between E_s and E_m set to 0.08333) and f_c, defined as (Ortiz-Suslow, Haus, Williams, Graber, & MacMahan 2018):

$$f_c = \frac{g}{2.4\pi U cos(\psi - D_p)}, \tag{14}$$

where g is gravitational acceleration (9.81 ms^{-1}), U is the local mean wind speed, ψ is the local mean wind direction, and D_p is the direction of the spectral wave peak. If $f_c <$ 0.125, then the sea state was assumed to resemble a bi-modal distribution with distinct swell (E_s) and windsea (E_w) bands only, i.e. $E_m = 0$. Values above 0.4 were fixed to $f_c = 0.4$ and this limit was only reached rarely when $U cos(\psi - D_p) \to 0$. These decisions were based on inspections of the directional wave spectra for the entire observing period of CASPER-West. During almost the entire experiment, there was very low frequency incident swell from south-southwesterly direction, a mid-frequency swell from the southwesterly-northwesterly, and a windsea from the west-northwesterly that developed almost every day. These wave conditions are typical of autumnal Southern California.

Several field studies have shown that the relative direction between the wind and dominant waves can help explain unexpected changes in wind stress and other parameters with time and/or space (Grachev et al. 2003; Ortiz-Suslow et al. 2018, 2015; Shabani et al. 2014; Zhang, Drennan, Haus, & Graber 2009). To account for this here, the relative angle between the wind direction (ψ) and mid-frequency swell peak wave directions (D_{pm}) was examined. Their relative angle ($R_m \equiv D_{pm} - \psi$) was classified into broad two sectors:

- $D_{pm} \sim \psi$: wind and swell aligned [-40°,40°],
- $D_{pm} \perp \psi$: cross-wind swell [40,140] & [-140,-40].

Initially, northerly and southerly winds were separated, but our analysis revealed that $D_{pm} \perp \psi$ for northerly winds only occurred during low wind speeds and were relatively infrequent. Therefore, all cross-swell wind conditions will be aggregated.

3.4 Screening Data for Stationarity

One of the key, underlying assumptions of the Reynolds decomposition is that $\mathbf{U}$ reflects the mean flow over the user-defined averaging window and that $\overline{\mathbf{u'}} \equiv 0$. These conditions rely on the statistical stationarity of the flow over the entire window length. Investigators can inspect the normalized cumulative summation and ogive to determine if a single flux sample (i.e. one averaging window) exhibits stationarity. This is a common practice in experimental turbulence and the reader is directed to French, Drennan, Zhang, and Black (2007) (Figure 7 therein) and Potter et al. (2015) (Figure 3 therein) for micrometeorological examples using aircraft and buoy observations, respectively.

The i^{th} value of the normalized cumulative summation of time series x (CS_x) can be defined as:

$$CS_x^i = \frac{\sum_{j=1}^{j=i} x_j}{\sum_{j=1}^{N} x_j} \tag{15}$$

where N is the number of realizations in x; the ogive is the normalized CS_x using the frequency-dependent power spectrum of x. The most direct means of confirming stationarity using these statistics can be through visual inspection. However, this was impractical for the *FLIP* datasets, which contained over 10,000 analysis windows for a 30-min average, and furthermore, visual inspection is inherently subject to observer biases. Ortiz-Suslow et al. (2019) carried out a visual inspection of a subset of the *FLIP* data to highlight the impact of averaging window. Using observation data, Martins, Miller, and Acevedo (2017) demonstrated that using empirical mode decomposition can help reduce the number of samples flagged as non-stationary in an eddy covariance dataset, though this method was not applied for the present study.

Here, we used $x = w'u'$ to screen the momentum flux profiles and $x = w'\theta'$ (θ is the sonic-derived potential temperature) to screen the temperature and moisture flux profiles. The standard deviation (σ) between an individual CS_x and the fraction of the averaging window length was assessed against a critical value (σ_c); if $\sigma > \sigma_c = 0.1$, then that sample was flagged as potentially non-stationary. This was done for each individual flux sample of each respective level of the *FLIP* mast. We use the qualifier, "potentially", because a comprehensive stationarity assessment cannot be done without assessing the ogive, however it is much easier to assess CS_x using automatic processing.

3.5 An Algorithm for Testing the Constant Flux Layer Assumption using *FLIP* Data

There is no standard approach to either testing or validating the presence of the constant flux layer. Aforementioned studies, where multiple three-dimensional sonic anemometer levels were deployed, have used various methods to evaluate their observed stress divergence; and single point measurement systems have no recourse for diagnosis. Theoretically, Tennekes (1973) provides a baseline from which to evaluate profile measurements, though this theory is inadequate to account for geophysical turbulence near a wavy boundary.

For this analysis, we will use the total flux gradients of momentum, sensible and latent heat:

$$\tau(z) = \rho\, \mathsf{u}_{*z}^2 = \rho\, (\overline{\mathsf{w}'_z \mathsf{u}'_z}^2 + \overline{\mathsf{w}'_z \mathsf{v}'_z}^2)^{1/4}, \tag{16}$$

$$S(z) = \rho C_p \overline{\mathsf{w}'_z \theta'_z}, \tag{17}$$

$$L(z) = \rho L_e \overline{\mathsf{w}'_z \mathsf{q}'_z}, \tag{18}$$

where ρ is the moist air density (from version 2 of the air-sea toolkit: `https://www.usgs.gov/software/sea-mat-matlab-tools-oceanographic-analysis`) and θ and q are the potential temperature and specific humidity, respectively. C_p is the specific heat of dry air at constant pressure (from COARE 3.5: $C_p = 1004.67\, J/kgK$) and $L_e = 10^3(2500.8 - 2.36\Theta_s + 0.0016\Theta_s^2 - 0.00006 \times \Theta_s^3)$ is the latent heat of evaporation using the mean radiometric sea surface temperature, Θ_s (from Table 2.1 in Rogers & Yau 1989). The above relations are the total *local* flux, but herein the explicit z-dependence will be dropped for simplicity. Also, the $'$ used in 16-18 denotes the linearly detrended and demeaned x, which includes both Reynolds and wave-coherent components.

Similar to Mahrt et al. (2018), we assumed that the flux gradient should vary linearly with z over the *FLIP* profile and we developed an algorithm to test the observed gradient against the linear model using least-squares regression: $y_i = mz + B$. Here y_i is the i^{th} profile of τ, S, or L and m and B are regression coefficients. For this study, we will focus on the estimated slope (herein m_o), which we will use to indicate the amount of divergence in the observations. A large $|m|$ indicates a divergent flux layer, whereas $|m| \to 0$ suggests the constant flux layer assumption is approximately valid.

It is important to emphasize that there was *always* a gradient the *FLIP* profiles. The aim of this study was to devise a threshold to judge each flux profile to determine which could be approximated as satisfying the constant flux layer assumption. The threshold we chose was $\pm 10\%$ from the height-median μ_z. We use the median because it is less sensitive to non-representative values. Therefore, for each profile to satisfy the constant flux layer, there is a maximum acceptable flux divergence. The slope of this threshold flux gradient was termed the expected slope, m_e:

$$m_e = \frac{(\mu_z + 0.1\mu_z) - (\mu_z - 0.1\mu_z)}{\Delta\, z} = \frac{0.2\mu_z}{\Delta\, z}. \tag{19}$$

Thus, m_e is calculated adaptively for each analyzed profile and $\Delta\, z$ is the difference in altitude between the highest and lowest flux level. The sign of m_e was fixed to the sign of m_o and m_o was compared to m_e using the index:

$$m_r = \frac{m_e - m_o}{m_e}. \tag{20}$$

Essentially, for profile i to be considered constant, it must not exhibit a linear slope (m_o) larger than a linear slope of a 20% monotonic change in flux from the bottom to the top of the observation range (m_e). If $m_r > 0$ ($m_r < 0$), i passes (fails) this test and the given profile is considered constant (divergent). Using this index allows us to systematically evaluate the prevalence of the constant flux layer ($m_r > 0$) and how this varies with MASL forcing. m_r is a skewed distribution, given that as $m_o \to 0$, $m_r \to 1$, but $m_r \to -\infty$ for divergent profiles. The value of m_r is not the focus of this paper, but it is indicative of the observed flux gradient. For example, $m_r \;\; -1$ indicates that the observed flux gradient is $2\times$ larger than expected and for $m_r \;\; -10$, the observed flux gradient is an order of magnitude larger than expected. Practically, $m_r \neq 0$, but this reference line will be used to demarcate the constant flux ($m_r > 0$) and divergent flux ($m_r < 0$) gradient regimes. For clarity in plotting, the lowest limit of m_r will usually be cut-off at -10, unless otherwise stated.

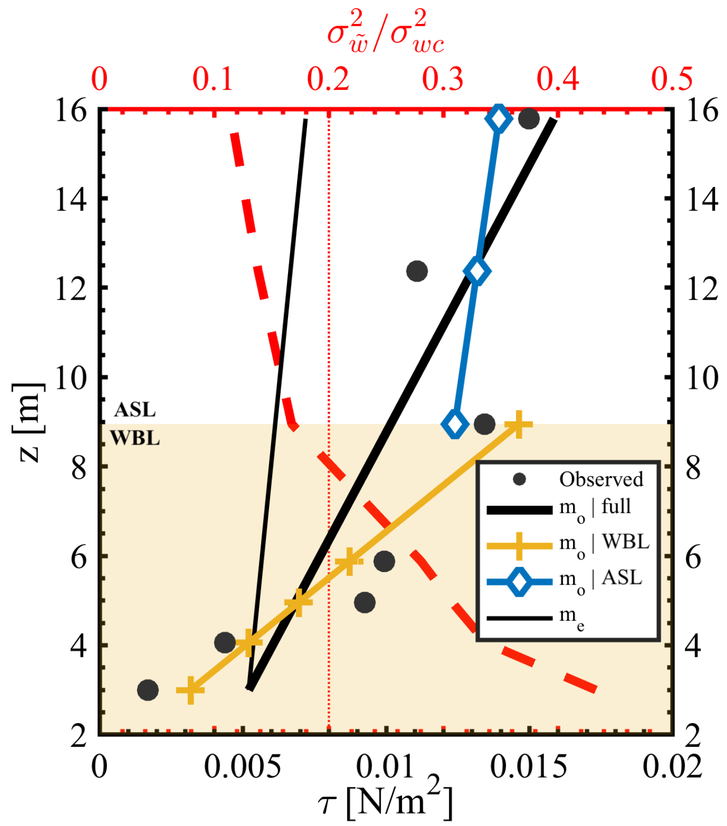

Figure 3. An example of the regression analysis using τ. The observations (black dots) are used to estimate the linear slope (m_o) of the stress gradient (thick black line), which is compared to a gradient with an expected slope (m_e, thin black line), see eqn. 19. These slopes are directly compared using the index m_r, eqn. 20. In addition to analyzing the full profile, the method outlined in section 3.2 was used to demarcate the WBL from the ASL and the linear regression was applied within these sub-layers independently. In other words, an independent estimate of m_o is derived for the full, ASL, and WBL profiles and these will be the foci of the analyses in the following sections.

Linear regression was applied to the full profile, as well as the vertical ranges of the ASL and WBL defined by z_{wbl} using the HHF analysis (see Figure 3 for example for τ). If z_{wbl} was larger than the top of *FLIP*'s mast, then we determined that we did *not* observe the ASL. In other words, wave-coherent turbulence ($\tilde{x}$) dominated the Reynolds stresses for the entire mast height. The converse scenario (i.e., no WBL observed) also occurred. For both cases, the null condition also contained cases where the ASL or WBL occupied only 1 measurement level.

The momentum and heat flux gradients were each partitioned between the WBL and ASL and analyzed using the method outlined above. Theoretically, we expect that the wave-coherent motion should not have a significant impact on the scalar turbulence (Sullivan, Banner, Morison, & Peirson 2018), but recent numerical studies have shown that surface waves can impact the turbulent scalar transport (Yang & Shen 2017). Thus, comparing the prevalence of scalar flux divergence in the WBL and ASL may be useful in providing some insight to this open debate.

4 Results

Here, the results of applying the constant flux layer test for the entire *FLIP* dataset are summarized. Over 1500 individual profiles passed the various levels of QC in the initial post-processing, including a criteria developed for CASPER-West that removes data subject to significant flow distortion. Before analyzing, all flux levels were individually tested for non-stationary conditions and only profiles where all flux levels passed this test were considered *stationary*. Due to the limits of our automatic stationarity screening, the results below will show the complete dataset along-side results from the stationary subset. Here, the total flux profiles for τ, S, and L were analyzed using the empirical algorithm outlined above (Section 3.5). The relationship between the HHF analyzed and observed turbulence was only used to determine z_{wbl}. Since the total flux is used, our hypothesis is explicitly stated as: the flux profiles for momentum, temperature, and moisture are non-divergent ($m_r > 0$) across the full profile, WBL, and ASL vertical spans.

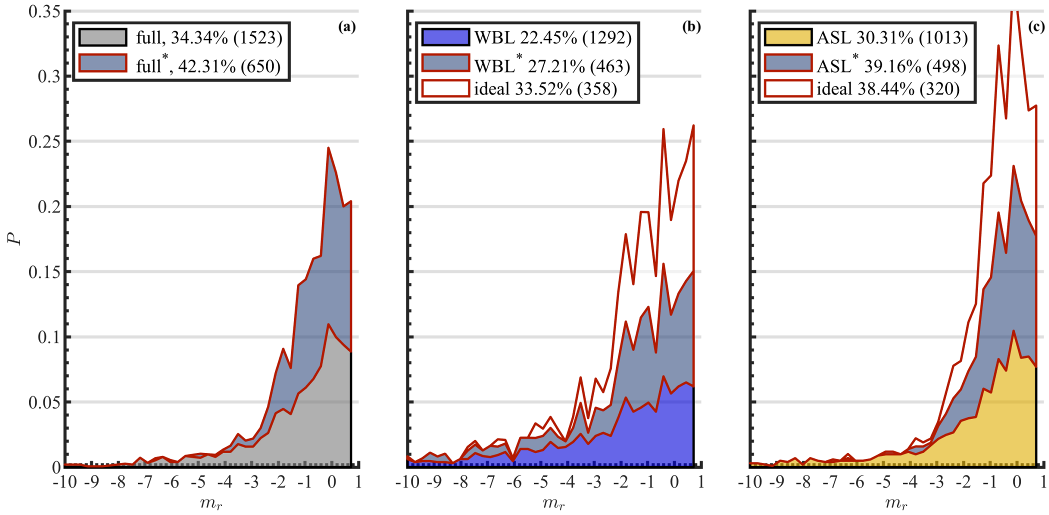

Figure 4. Probability distributions, P, of m_r for τ over the (**a**) full, (**b**) WBL, and (**c**) ASL profiles, respectively. Here, * indicates cases where the entire profile was considered stationary. The “ideal” subset occurred when stationarity was concurrent with a substantial ASL, or WBL, defined as a layer spanning at least three measurement levels. Within each panel, the P have been stacked. For each subset, the proportion of profiles where $m_r > 0$ are given, alongside the total number of profiles analyzed in the various subsets.

4.1 The Constant Flux Layer for Momentum

The probability distributions, P, of m_r calculated using τ, were rather unexpected. For the full profile results (Figure 4a), the cumulative probability of $m_r > 0$ was about 34%, which increased to 42% if only considering stationary conditions. However, by accounting for stationarity, we effectively reject more than 50% of our entire dataset, indicating that the MASL is more often non-stationary. The rates of data loss were somewhat surprising, but similar rates have been reported in other marine micrometeorological datasets (Martins et al. 2017).

The general pattern noted in the statistics of the full profile results held in both the WBL and ASL, with the latter exhibiting ~10% more profiles where $m_r > 0$. For the ASL and WBL, accounting for stationarity increased the proportion of profiles where $m_r > 0$, but at the cost of 51% and 64% of the overall WBL and ASL datasets, respectively (Figures 4bc). It was noteworthy that an ASL could only be defined for 1013 profiles, or about 2/3 of the entire *FLIP* dataset. Likewise, there were cases when no WBL could be defined, but there were substantially fewer of these cases. We defined the subset of the data as "ideal" when stationarity was concurrent with a sufficiently thick WBL or ASL. "Thick" was defined as spanning at least three measurement levels. Focusing on "ideal" conditions had a substantial impact on P for the WBL (Figure 4b), but had a negligible impact on the ASL results(Figure 4c). In summary, our results indicate that, under stationary conditions, the total momentum stress profile only satisfied the constant flux layer assumption approximately 30% and 40% of the time in the WBL and ASL, respectively.

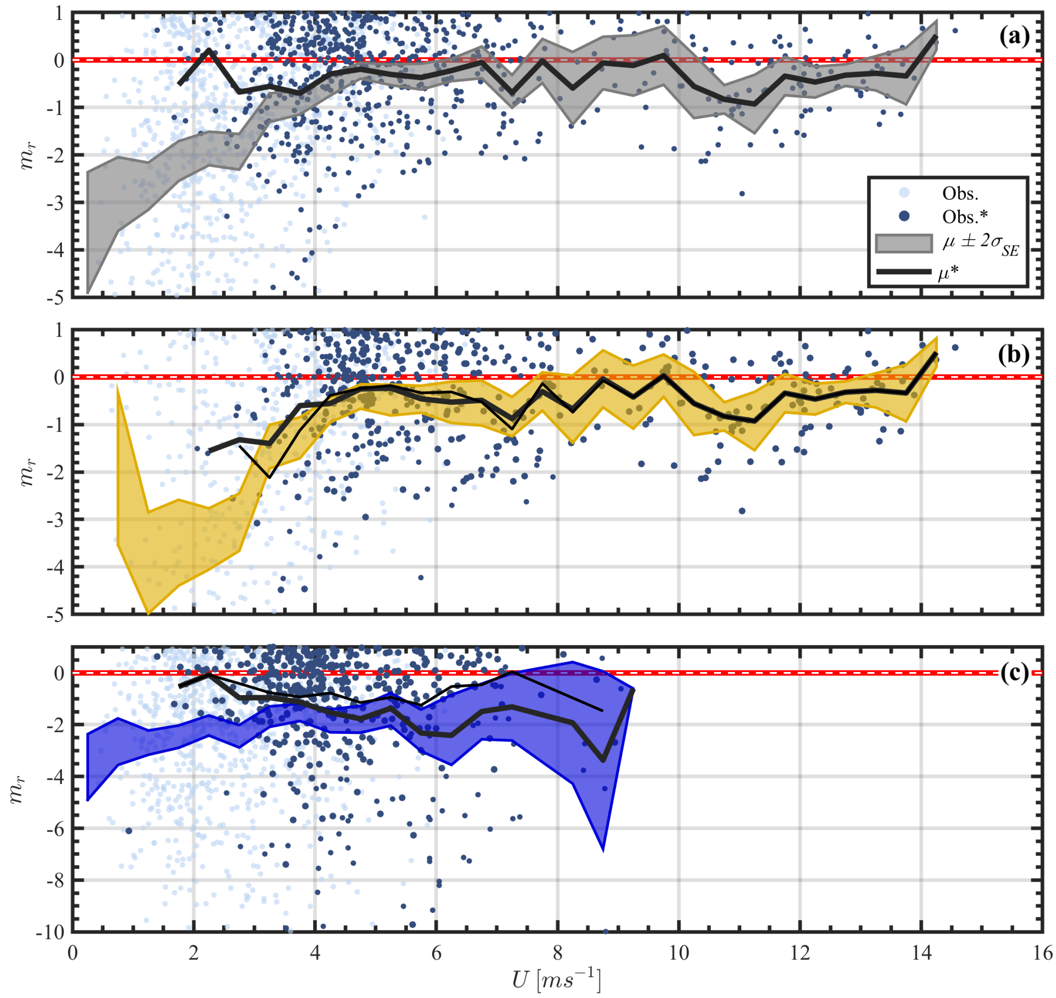

Figure 5. Distributions of m_r (from τ) as a function of the vertically-averaged wind speed, U for the full (top), ASL (middle), and WBL (bottom) profiles, respectively. Note the change in vertical scale between lower and upper-middle panels. U-bin averaging with discrete bin width $= 1\ ms^{-1}$ was used to filter the distributions. For the complete data, the shading spans $2\times$ the standard error (σ_{SE}) and is centered on the mean, μ. For stationary and "ideal" conditions (thin black line), only the filtered μ is given.

We expected that the MASL state, namely the mean wind speed (U) and atmospheric stability (ζ), would have an impact on the stress divergence and thus be reflected in m_r. Theoretically, divergence should be prevalent in very low winds, both as a result of low signal-to-noise ratio in the sonic anemometry and the dominance of buoyancy-driven turbulence and non-stationarity in this regime. For $|\zeta \to \infty|$, we expect divergence to be prevalent because of the importance of non-shear driven turbulence scales (Tennekes &

Lumley 1972). Note that each distribution of m_r was analyzed with respect to the vertically-averaged U or ζ over the corresponding vertical span (full, ASL, or WBL profiles).

In terms of U-dependence, the relationship was complex (Figure 5). A uniform, discrete bin-averaging scheme with a spacing of $\Delta U = 1$ ms^{-1} was used to filter out the considerable scatter in the distributions. For the ASL (and full profile) results, the filtered m_r exhibited a positive trend with U up to 4 ms^{-1}. Within the ASL, accounting for stationarity reduced the strength of this relationship, but a roll-off in m_r was still observed below 4 ms^{-1} (Figure 5b). Note that stationarity was essentially limited to $U >$ 2 ms^{-1}. Beyond 4 ms^{-1}, the filtered m_r exhibited no wind speed dependence, converging on $m_r \sim -0.3$. The only significant crossing of the $m_r = 0$ line occurred above 14 ms^{-1}, the data of which came from the passage of an atmospheric front during CASPER-West. Stationarity and "ideal" conditions had no discernible effect on the mean trend of m_r within the ASL beyond 4 ms^{-1} (Figure 5b).

The wind speed dependence within the WBL differed from the results for the full and ASL profiles (Figure 5c). For the filtered m_r, there was no significant wind speed dependence for any span of U. However, for stationary or "ideal" profiles we found a conflicting trend. Whereas m_r derived from stationary profiles trended negatively with U ($r^2 = 0.48$, $p = 0.012$), this disappeared for "ideal" profiles. We also observed that the mean m_r for "ideal" profiles was substantially closer to $m_r = 0$ than for either the complete or stationary distributions.

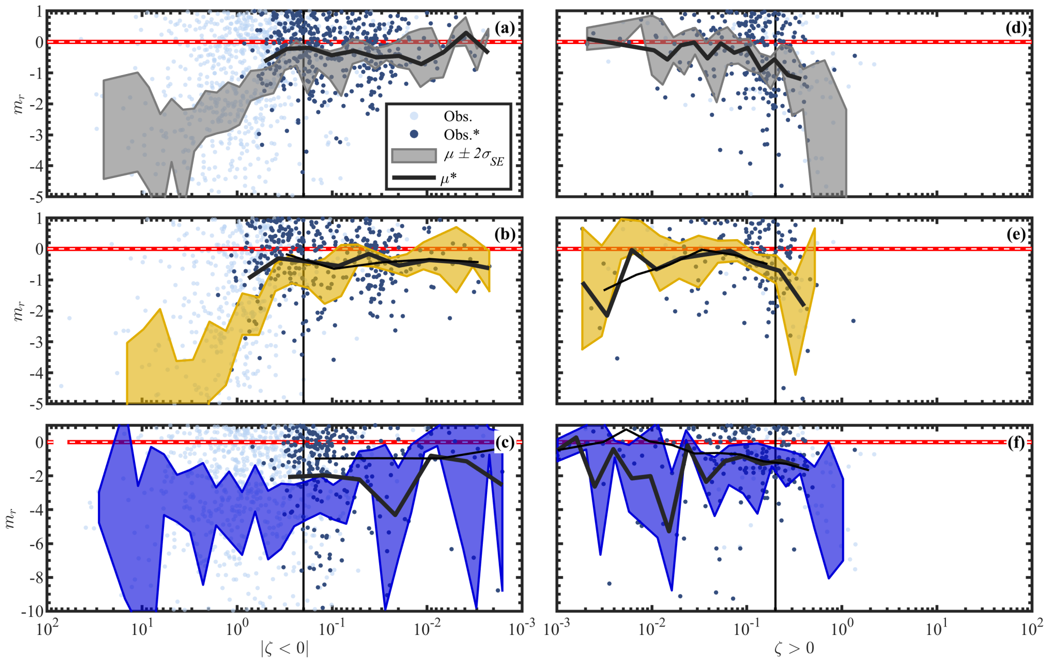

Figure 6. Same as Figure 5, but for the dependence on stability, ζ. The data under unstable (left column) and stable (right column) conditions are shown. The log-scaled bin-averaging scheme, with a uniform bin width, was performed over a fixed range of $10^{-3} < |\zeta| < 10^2$. Due to significantly more samples from $\zeta < 0$, the bin width for unstable conditions was larger (roughly 2×) than for stable conditions. The vertical lines mark $|\zeta| = 0.2$.

The dependence of m_r on ζ was also explored using a similar technique (Figure 6). For the ASL (and full profile) results, essentially all profiles exhibited $m_r \to -\infty$ for $|\zeta| >$ 1 (Figure 6ab-de). While stationary conditions were not observed beyond $|\zeta| \approx 1$, m_r from stationary (and "ideal") profiles suggests a roll-off in m_r in the transition to a strongly (un)stable MASL. For moderately unstable to near-neutral conditions ($\zeta \to -0$), the

ASL flux gradients were not dependent on ζ (Figure 6b). For the stable ASL, a distinct peak around $\zeta = 0.1$ was observed (Figure 6e). Also, we observed no difference between the observed, stationary, and "ideal" profiles. We should emphasize that the overall paucity of individual samples under stable conditions within the ASL adds uncertainty to the representativeness of these results. Within the WBL, m_r reflected no dependence on ζ. A possible exception is within the WBL when $0 < \zeta < 0.2$, where a slight negative trend in m_r ($r^2 = 0.62$, $p < 0.01$) was observed (Figure 6f).

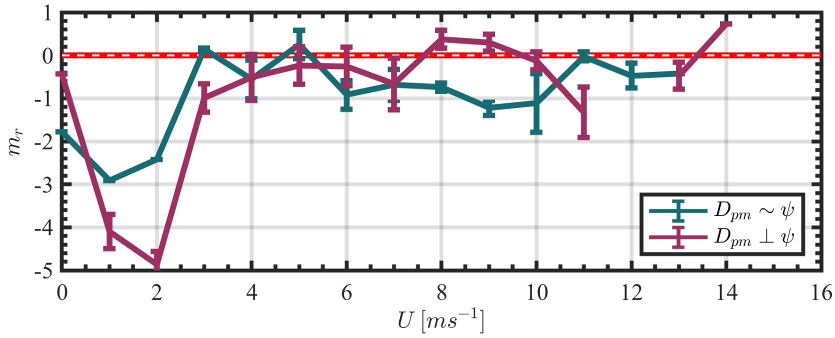

Figure 7. Similar to Figure 5b, but m_r has been separated into cases with swell-wind alignment ($D_{pm} \sim \psi$) and cross swell-wind ($D_{pm} \perp \psi$). At each 1 ms^{-1} bin, the mean m_r was calculated only for range of stabilities near neutral, $-0.5 < \zeta < -0.5$. Error bars span 1× the standard deviation. Only results within the ASL are shown.

Figures 4-6 reflect a complex picture of the constant flux layer model within the MASL. While stationarity explains much of the variance of m_r in low winds, the unexpected finding was the persistence of divergent flux for U above 4 ms^{-1} (Figure 5b). To address this, the dependence of m_r on the relative direction between the dominant waves and the wind vector direction ($R_m \equiv D_{p,m} - \psi$) was investigated. Here, *dominant* was chosen to be the wave direction at the peak of the mid-frequency swell band, as observed from a nearby directional wave buoy (see Section 3.3). We emphasized using R_m, rather than other common wave statistics, to limit the co-linearity with U or u_*. Also, while defining z_{wbl} accounts for the wave-coherent turbulence, we expect that the flow over varying surface geometries could still impact the total stress gradient above the WBL. The mechanisms for this effect has been suggested through observations in both depth-limited and deep water regimes (Grachev et al. 2003; Ortiz-Suslow et al. 2018; Potter 2015; Shabani et al. 2014).

Only using the ASL profiles, the impact R_m has on the U-dependence of m_r was analyzed (Figure 7). Also, because Figure 5b revealed no difference between the observed and stationary profiles for $U > 4$ ms^{-1}, the impact of R_m is shown for the observed results. To simplify the analysis, swell-wind directions were classified into aligned ($D_{pm} \sim \psi$) and cross ($D_{pm} \perp \psi$). For $U < 4$ ms^{-1}, under both cases of wind-swell alignment, $m_r << 0$, with $D_{pm} \sim \psi$ being associated, on average, with stronger flux divergence in the MASL. For $4 < U < 6$ ms^{-1}, R_m had no impact on m_r. However, beyond 6 and up to ∼10-12 ms^{-1}, R_m for the two cases diverge and bi-furcate along the $m_r = 0$ line. Here, flux divergence was associated with swell-wind alignment, whereas non-divergence was associated with $D_{pm} \perp \psi$. Beyond this regime, the data come from one particular atmospheric event and may not be generally representative. This indicates that the persistent $m_r < 0$ observed in Figure 5b, for wind speeds between 5 and 12 ms^{-1}, was associated with cases of surface wind alignment with the dominant swell waves.

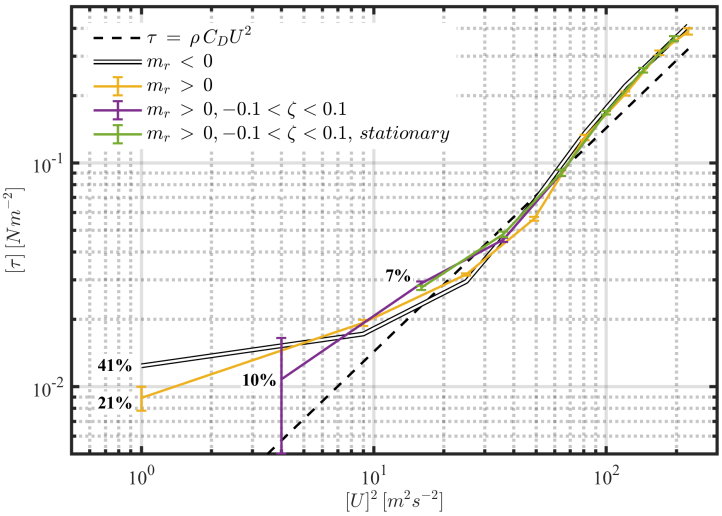

Figure 8. Wind dependence of $[\tau]$, the aggregate mean over height and wind speed (2 ms^{-1} bin-average), for four subsets of the *FLIP* data. These data only include observations made within our empirically defined ASL. We have provided a $\tau\, v.\, U^2$ using a constant $C_D = 0.0012$ and $\rho = 1.196$. Given along-side each curve are the percent of all the *FLIP* flux profiles analyzed for this study.

4.2 Surface Wind Stress in the Constant Flux Layer

Using the results from m_r evaluation, we analyzed the wind dependence of the total wind stress from *FLIP* within the defined ASL (Figure 8). The stress, τ, is related to the wind speed through the drag law, $\tau/\rho = u_*^2, = C_D U^2$. Ideally, τ should linearly depend on U, but it is well-known that the aerodynamic drag of the ocean surface (C_D) is a complex function of many factors, including wind speed. For this analysis, we will define the aggregated mean, [], as the result of averaging over the height of the ASL and applying a 2 ms^{-1} bin-average with wind speed.

$[\tau]$ for the divergent ASL ($m_r < 0$) exhibited a non-linear dependence with $[U]^2$ and become relatively insensitive to $[U]^2 < 10\ m^2 s^{-2}$. This behavior resembles the "hockey stick" shape reported for u_* in many field datasets (Mahrt et al. 2018), which results in $\tau \neq 0$ when $U \to 0$. Using linear extrapolation, we found that $[\tau([U]^2 = 0)] = 0.01$ for the divergent ASL. If only considering non-divergent profiles ($m_r > 0$), we found more sensitivity to wind with decreasing $[U]^2$. This sensitivity increased if only including non-divergent and near-neutral profiles. For these two cases, $[\tau([U]^2 = 0)]$ was 0.004 and -0.007, respectively. The latter indicating $[\tau] \approx 0$ at $[U]^2 \sim 1\, ms^{-1}$. For the non-divergent, near-neutral, and stationary ASL, the minimum $[U]^2$ was between 3-5 ms^{-1}, which reduces our confidence in extrapolating $[\tau]$ for these cases. However, the general trend agrees with the non-divergent and near-neutral results.

It is common to define a rule-of-thumb value for $(u_*/U)^2$, e.g., 0.0012 (W. G. Large & Pond 1982; Mahrt et al. 2018), especially for wind speeds $< 10\ ms^{-1}$. For the $[\tau]$ shown in Figure 8, the corresponding values for $(u_*/U)^2$ were 0.0012 and 0.0015 for the case of $m_r > 0$ and $m_r > 0\, \&\, |\zeta| < 0.1$, respectively—this was for $U < 6\ ms^{-1}$. For higher winds, we estimated a rule-of-thumb value to be 0.0013 and 0.0003, respectively. We also compared the observed total u_* to the results from the COARE 3.5 algorithm (J. B. Edson et al. 2013). In this analysis, we also apply the 2 ms^{-1} bin-average with wind speed, but the results across the different measurement levels. For this comparison, we excluded

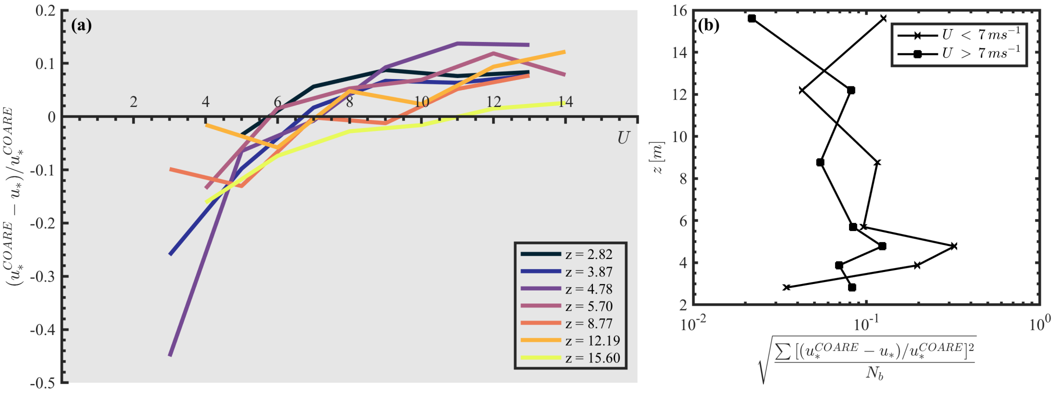

Figure 9. **(a)** Relative difference between observed and COARE-derived total friction velocity (u_*). Only cases where $m_r > 0$ and $-0.1 < \zeta < 0.1$ were included in the comparison. **(b)** Profiles of root mean square relative different for two wind regimes.

measurements made within the WBL, divergent fluxes, very low winds ($U < 2\ ms^{-1}$), and (un)stable conditions (i.e., only cases where $-0.1 < \zeta < 0.1$ were used). The equivalent friction velocity, u_*^{COARE}, was calculated using the bulk atmospheric measurements from the *FLIP* mast at the near 10-m altitude (the software version used to derive COARE variables is included in the supplemental material). Figure 9 summarizes this comparison by analyzing the wind speed (Figure 9a) and height (Figure 9b) dependence of the relative difference: $(u_*^{COARE} - u_*)/u_*^{COARE}$. We found systematic differences between the observed u_* and COARE as a function of wind speed, with the bulk-equivalent underestimating (over-estimating) the observations below (above) $\sim$7 ms^{-1}. For measured values below 4 ms^{-1}, COARE under-estimated u_* by as much as 40%. Above 7 ms^{-1}, the relative difference seems to level-off, though there is some indication of a weak dependence with increasing U. However, further data at higher winds would be necessary to confirm this. In this higher wind portion, we found that the disagreement with COARE decreased with altitude and at $z \sim 16$ m ($r^2 = 0.2$), the relative difference was within 5%. This relationship was not statistically significant ($p = 0.32$), which we attributed to the low number of data points.

4.3 The Constant Flux Layer for Temperature and Moisture

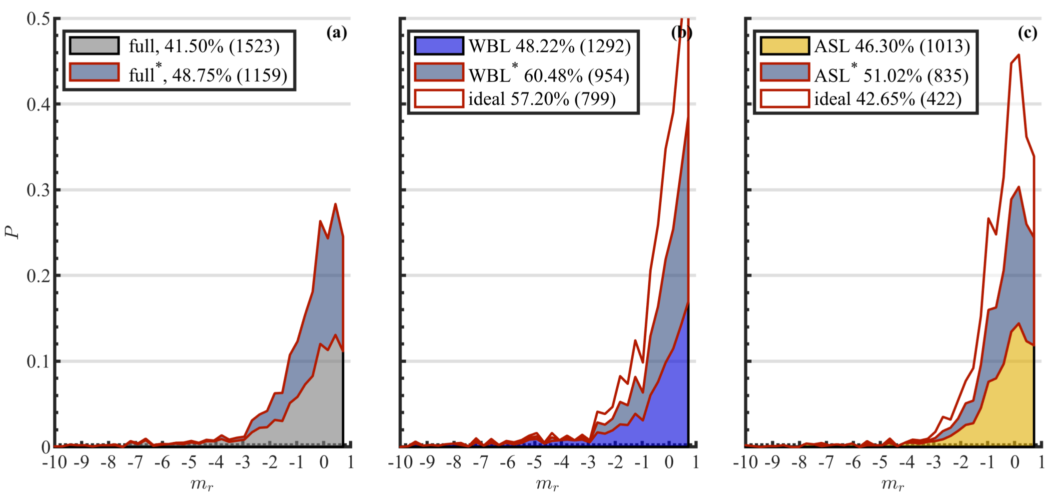

Figure 10. Probability distributions, P, of the m_r for S over the (**a**) full, (**b**) WBL, and (**c**) ASL profiles, respectively. Here, * indicates cases where the entire profile was considered stationary. The "ideal" subset occurred when stationarity was concurrent with a substantial ASL, or WBL, defined as a layer spanning at least three measurement levels. Within each panel, the P have been stacked. For each subset, the proportion of profiles where $m_r > 0$ are given, alongside the total number of profiles analyzed in the various subsets.

Prandtl's mixing theory implies that the diffusion of momentum and heat are proportional. We did not find a distinction in the literature between the constant flux layer for momentum and the constant flux layer for heat, therefore we approached the scalar flux gradients (S and L) similarly to momentum. For MOST, it is conventional to apply the same dimensionless gradient function for both temperature and moisture (J. Edson, Zappa, Ware, McGillis, & Hare 2004; J. B. Edson & Fairall 1998), therefore our hypothesis was that the results between temperature and moisture would (1) be similar to the findings of τ and (2) be similar to each other. Figures 12 and 13 summarize the results of m_r using S and L, respectively.

In general, the constant flux layer was more often found for the heat fluxes than for momentum, with nearly 50% and 60% of S and L full profiles being non-divergent under stationary conditions (Figures 12a-13a). Furthermore, we found that 75% of the heat flux profiles passed the stationarity test using $C_{w'\theta'}$, which was in stark contrast to momentum. For S within the ASL, $m_r > 0$ for 51% of profiles (Figure 12c). Unlike for τ, within the WBL flux divergence of S was *less* likely than within the ASL, with over 60% of WBL profiles (versus 50% within the ASL) satisfying the constant flux layer assumption (Figure 12b). Within the ASL, the $m_r > 0$ was less likely under "ideal" conditions, where the proportion of non-divergent profiles drops by nearly 10% relative to simply stationary conditions (Figure 12c). This effect was not as significant within the WBL (Figure 12b).

For L, this general pattern held (Figure 13), in that non-divergent flux gradients were found more often within the WBL than in the ASL, regardless of stationarity or an "ideal" profile (i.e., a profile spanning at least 3 measurement levels). However, for L, there were some slight differences when comparing the results of S. Within the WBL, ≈50% of profiles exhibited $m_r > 0$, with only minor changes in this proportion if only considering stationary or "ideal" profiles (Figure 13b). Within the ASL, only 38.5% of profiles passed the $m_r > 0$ test, but this increased to 50.5% under "ideal" conditions (Figure 13c). The analysis of L is limited in that there were only 5 measurement levels available due to (assumed) contamination of two of the gas analyzer surfaces.

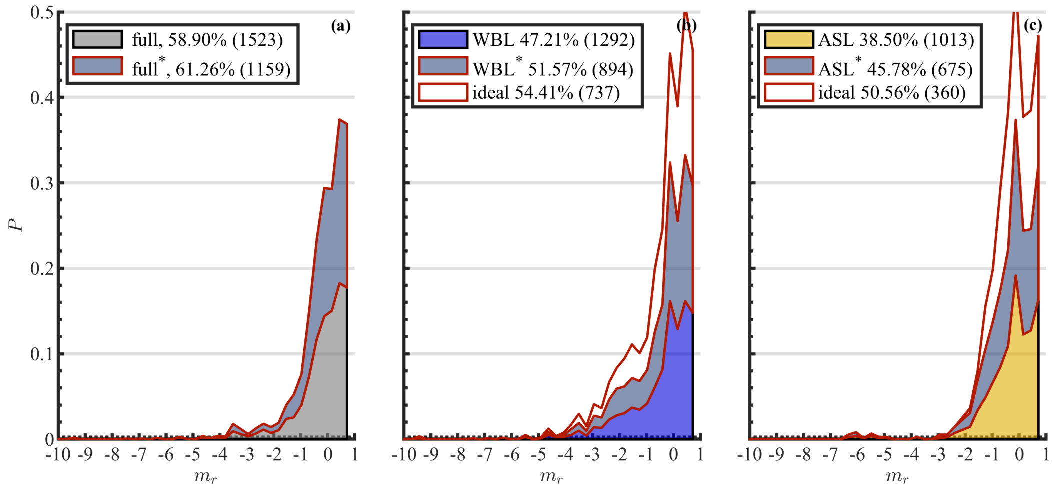

Figure 11. Probability distributions, P, of the m_r for L over the (**a**) full, (**b**) WBL, and (**c**) ASL profiles, respectively. Here, * indicates cases where the entire profile was considered stationary. The "ideal" subset occurred when stationarity was concurrent with a substantial ASL, or WBL, defined as a layer spanning at least three measurement levels. Within each panel, the P have been stacked. For each subset, the proportion of profiles where $m_r > 0$ are given, alongside the total number of profiles analyzed in the various subsets.

Apart from impacts of stationarity, profile length, and wave-coherent motion (WBL v. ASL), we tested m_r for S and L against the bulk air-sea temperature difference ($ASTD$). Here, $ASTD$ was defined as the air temperature, using a mean of the lowest four bulk temperature probes on the mast, minus the sea surface skin temperature (SSST)—the latter acquired radiometrically (see Ortiz-Suslow et al. 2019). For S within the ASL, we found that m_r was negatively proportional to $ASTD$ over the range $[-4, -1]$, i.e., the convection regime. While this trend is difficult to discern in Figure 12b because of the vertical axis range, it was fairly strong and statistically significant in both the complete and stationary-filtered subsets ($r^2 = 0.57$, $p = 0.004$ and $r^2 = 0.41$, $p = 0.03$, respectively). A similar relationship was found within the WBL, but with the trend only becoming evident at $ASTD \sim -2°$ C (Figure 12c).

As $|ASTD| \rightarrow 0$ all of the profiles analyzed contain a distinct local minima (or trough) in the complete datasets. This trough is all-but removed by screening non-stationary profiles. In our initial analysis, this trough persisted in the stationary and "ideal" when our screening applied the results for the $w'u'$ to momentum and heat. Using a temperature-dependent stationarity analysis removed this distinct signal from the distributions of m_r for S. For stable conditions ($ASTD > 0$), there is a suggestion that increasing $ASTD$ is associated with increasing m_r, but the limited sample size under this regime makes analysis challenging. This was the case within both the ASL and WBL.

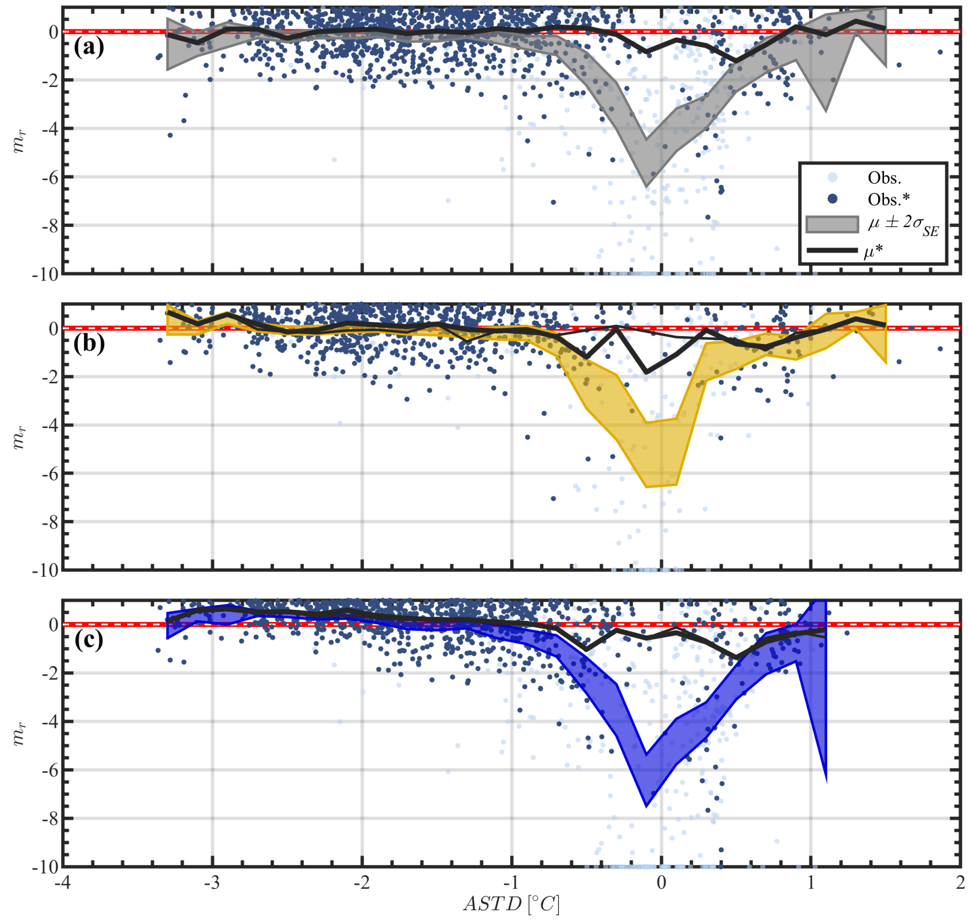

Figure 12. Distributions of m_r (from S) as a function of $ASTD$ for the full (**a**), ASL (**b**), and WBL (**c**) profiles, respectively. The thin black line represents the filtered curve for "ideal", but in (**c**) this is occluded by the curve for μ^*.

The dependence on $ASTD$ was also investigated for L (Figure 13). Upon initial inspection, none of the sub-profiles analyzed exhibited a clear dependence or trend with $ASTD$. Furthermore, there was no indication of the non-stationarity-associated divergence evidenced in S by the near-neutral trough in Figure 12. However, we did find that within the ASL (Figure 13c) there was a distinct transition in the mean m_r about the limit $ASTD \sim -0.75°$ C. Over moderate-strongly unstable conditions ($ASTD < -0.75$), the mean m_r is negative and flux divergence was more prevalent. With increasing $ASTD$ through neutral to stable conditions, on average $m_r > 0$ and the constant flux layer is more generally satisfied. The separation of m_r about this limit was found to be significant using a student's t-test ($p = 0.001$). Within these two regimes of $ASTD$, we found that m_r did not exhibit any linear dependence on stability ($r^2 < 0.01$). Within the WBL, there was evidence of a transition in m_r with $ASTD$, but the limit was shifted by ~-1° C and the noise at the limit of the data range inhibits conducting a meaningful statistical analysis within the WBL. Similar to S, we found little influence of accounting for "ideal" conditions.

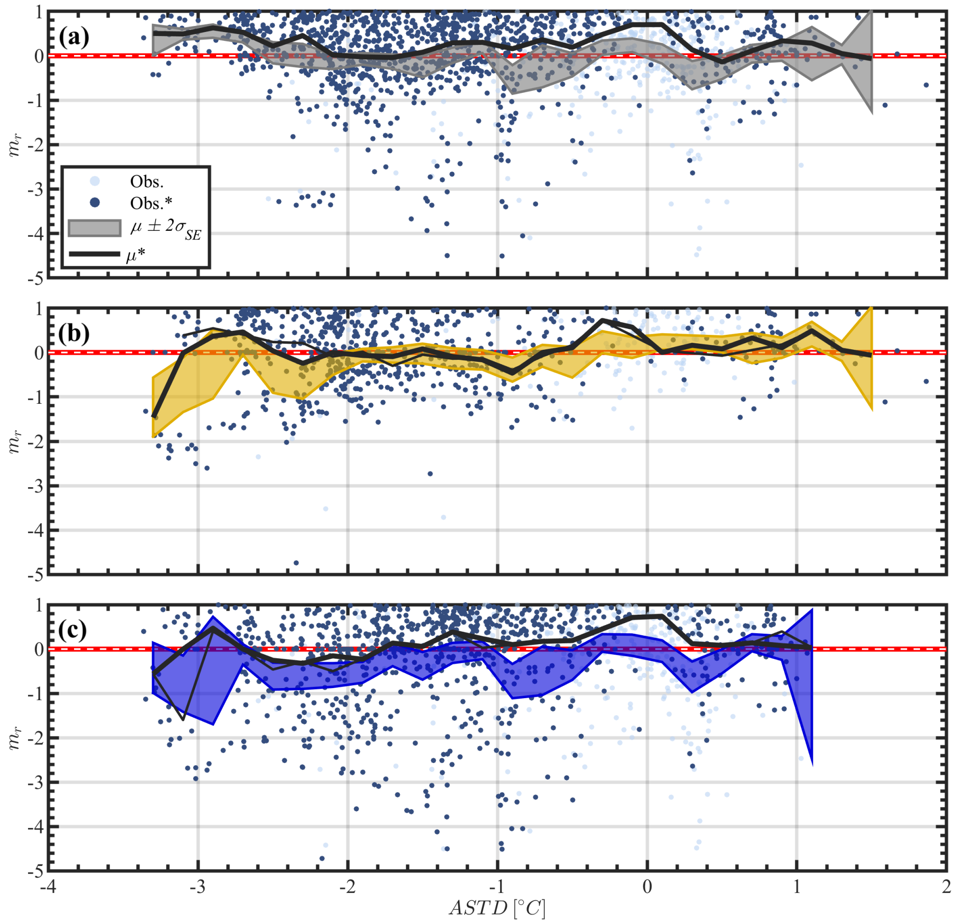

Figure 13. Same as Figure 12, but for L.

5 Discussion

One of the central findings of analysis was that stationarity plays a significant role in the flux gradients. In fact, stationarity largely explained the variance of m_r (for τ) at $U < 4$ and for $\zeta < -0.2$ (the most prevalent conditions from CASPER-West). However, only analyzing stationary flux conditions (where the entire profile was stationary) required excising ~60% of the entire dataset. Our stationarity test only used the homogeneity of the along-wind flux accumulation, which is an incomplete characterization of stationarity (French et al. 2007; Ortiz-Suslow et al. 2019; Potter 2015). However, C_x is relatively straight-forward to apply in an automatic processing algorithm and we would expect even *more* samples to be rejected if conducting a complete stationarity analysis. We also found that the stationarity of momentum and temperature flux were very different, with the latter be far more likely within the MASL. Independently assessing the momentum and heat flux stationarity had two distinct impacts: (1) enabling us to retain at least 50% more S and L profiles than τ, and (2) clearly explaining a strong and persistent signal in the relationship between S and $ASTD$ under near-neutral conditions (Figure 12). We had not found a previous field data set where the flux accumulation for momentum and temperature were treated independently for quality controlling the eddy covariance fluxes.

The interface between the WBL and ASL was empirically defined using the vertical gradient of wave-coherent air motion signal buried in the observed vertical velocity variance. This was used to partition the total flux gradients into WBL and ASL portions. From this, we found that the WBL height was quite dynamic over the CASPER-West time period. Our estimates of the WBL depth spanned the observation range of the *FLIP* mast (3-16 m) and depended on the local atmospheric and wave state. This range of altitudes is in-line with the theoretical framework developed by Chalikov and colleagues (e.g. D. Chalikov 1995; D. Chalikov & Rainchik 2011; D. V. Chalikov 1978; D. V. Chalikov & Makin 1991) and other observations (Grare et al. 2013; Smedman et al. 1999), but conflicts with the WBL depth hypothesized by Hristov and Ruiz-Plancarte (2014) and reported recently from the Southern Ocean (Cifuentes-Lorenzen et al. 2018). The WBL is an important sublayer within the MASL that holds import for wave modeling and air-sea flux measurement. Resolving these conflicts lies beyond the scope of the present study, but this problem requires further, focused attention from both theoretical and experimental perspectives.

Using the results from our evaluation of m_r for τ, we compared the wind speed dependence of u_* and the parameterized (COARE) value. If including non-divergent flux and near-neutral conditions, we found that the *FLIP* observations were within $\sim$20% of COARE. However, these differences were non-random. In particular, we found that COARE under-estimates u_* at low wind speeds ($U < 7$), which represents 2/3 of the CASPER-West data. This may not be surprising given the known deficiencies of bulk parameterizations at low winds (see Högström et al. 2018). In higher wind speeds, COARE tended to over-estimate u_*, but this disagreement tended to be worse closer to the surface. This suggests that while $m_r > 0$, the vertical stress gradient is non-random and near-surface fluxes may be systematically different from their bulk-equivalent values.

While stationarity played a significant role in the flux divergence at low winds, one of the puzzling findings was that divergent flux was prevalent with increasing wind speed within the ASL. We found that this was linked to the wind-swell relative direction (Figure 7ab). In particular, we found that when the wind vector and dominant swell were aligned, stress divergence was more prevalent in the ASL. This suggests that the air flowing across the wave crests imparts an additional turbulence velocity scale that interacts with, but is not solely dependent upon, the larger scale wind shear within the ASL. This additional, non-negligible scale necessarily breaks down the simplistic constant flux layer model. Recently, Ortiz-Suslow and Wang (2019) found that near the wavy surface inertial turbulence may exhibit non-Kolmogorov statistics. This was hypothesized to be attributed to wind shear-wave interactions injecting additional turbulence kinetic energy that could not be attributed to the wind shear-driven u_*. These independent studies may have captured different outcomes of the same phenomena and a more detailed study linking these two findings is necessary.

We found that the constant flux layer for temperature and water vapor was more often found in the WBL than the ASL, especially when comparing stationary flux conditions. Furthermore, we found that the dependence of m_r (for S and L) on $ASTD$ did not change between the WBL and ASL, respectively. These findings counter the results for the flux divergence in τ. This suggests that wave-coherent motion does not play a significant role in the scalar flux gradients. We also found that that the constant flux layer for temperature was slightly more prevalent than for water vapor, but that the former was highly sensitive to the turbulence stationarity. This could provide some justification for developing unique non-dimensional ϕ functions (equation 1) for mean gradients of temperature and water vapor, respectively.

It is important emphasize that our findings hold implications for characterizing turbulence on both sides of the interface. Scully, Trowbridge, Sherwood, Jones, and Traykovski (2018) explored near-bed turbulence over the inner continental shelf using the eddy covariance method and had to account for the presence of stress divergence in their analysis. It is possible that applying a similar approach as ours to the study of in-water turbulence, both near the bed and the interface could be helpful in more accurately characterizing these complex dynamics. Furthermore, the advent of very-near-the-surface air-sea flux platforms (e.g. Gentemann et al. 2020; Thomson, Girton, Jha, & Trapani 2018; Yamaguchi, Wang, & Kalogiros 2020) are providing critical new flux data close to a surface that is traditionally difficult to observe directly. Furthermore, these (semi)autonomous platforms are increasingly being deployed for long durations where automatic processing is being done on-board and processed parameters are being distributed quasi-instantaneously for consumption and assimilation. Understanding how the estimates of stress and air-sea fluxes derived from these platforms within the WBL relate to the flux across the entire MASL will be critical to appropriately entraining this measurements to help develop new insights into atmosphere-ocean coupled process studies.

6 Conclusions

The constant flux layer model, as applied to the study of the mean and turbulence variability within the MASL, is an idealistic concept that simplifies the problem of characterizing air-sea fluxes and mean gradients above the ocean surface. While the limits of this model are theoretically expected, a comprehensive validation has not been conducted within the marine environment. Nonetheless, it is applied and relied upon ubiquitously in observational studies of MASL processes. Using an extensive dataset collected from the unique *FLIP*, we employ a novel empirical approach to critically evaluate the statistical prevalence of the constant flux layer within the observed MASL for the flux gradients of momentum, temperature, and moisture. Central to our method was filtering out the wave-coherent motions from the ultrasonic anemometer using this information to empirically define the interface between the WBL and ASL.

In general, our results suggest that the natural variability within this near-wall region of the MASL is much larger than the conventional 10% margin, especially for the momentum flux. We found that less than 1/3 of momentum flux profiles could be approximated as non-divergent, this increased to ∼40% if only including statistically stationary flux profiles at the cost of approximately 2/3 of the dataset. The prevalence of momentum flux divergence for winds $6-12\ ms^{-1}$ was linked with wind-swell alignment, whereas non-divergent flux coincided with cases of wind and swell being perpendicular. The constant flux layer was more prevalent for the heat fluxes and ∼60% profiles were non-divergent (for stationary conditions). For sensible and latent heat, we found that the flux profiles within the WBL were more likely to be non-divergent as compared to the ASL, suggesting that the constant flux layer for heat is closer to the surface, as opposed to momentum which tends to be above the WBL.

Using our method, in order for at least 2/3 of momentum flux profiles to satisfy the constant flux layer, we would have to accept upwards of 40% relative difference between the flux levels on the *FLIP* mast. This poses a significant challenge to typical marine micrometeorological practices that rely on single point-based measurements made within 10 m of the ocean surface and assume the local stress is equivalent to the surface stress necessary for applying MOST. We emphasize that our findings suggest that much of the flux divergence within the MASL was non-random, indicating that even if successive levels fall within a threshold value (e.g. 20%), there can be systematic flux differences with altitude. For the local gradients, the impact might not be substantial in absolute value, but these differences become more significant when integrated over long time periods or large spatial distances.

Acknowledgments

This research was funded by the Office of Naval Research (ONR) Grant N0001418WX01087 under its Multidisciplinary University Research Initiative (MURI). We acknowledge and appreciate Denny Alappattu for his effort in guiding the early conceptualization of this study and in contributing to an early draft of this article. This work would not have been possible without the tremendous efforts given by Captain Tom and the crew of the *FLIP*. The CAPSER-West field work was supported by members of the NPS Boundary Layer Processes team: Alex Olson, Ben Wauer, Kyle Franklin, Anna Hook, and Richard Lind. Kirstin Paulsson, Tony de Paolo, and the Coastal Observing R & D Center, at Scripps Institution of Oceanography, are acknowledged for their efforts in collecting and processing the wave buoy data used in this analysis. The data used to conduct the analysis in this article are available at: https://calhoun.nps.edu/handle/10945/66510.

References

Anctil, F., Donelan, M., Drennan, W., & Graber, H. (1994). Eddy-Correlation Measurements of Air-Sea Fluxes from a Discus Buoy. *J. Atmos. Ocean. Technol.*, *11*, 7.

Andreas, E., Mahrt, L., & Vickers, D. (2014, sep). An Improved Bulk Air-Sea Surface Flux Algorithm, Including Spray-Mediated Transfer. *Q. J. R. Meteorol. Soc.*, n/a–n/a. Retrieved from `http://doi.wiley.com/10.1002/qj.2424` doi: 10.1002/qj.2424

Batchelor, G. K. (1947, oct). Kolmogoroff's theory of locally isotropic turbulence. *Math. Proc. Cambridge Philos. Soc.*, *43*(04), 533. Retrieved from `http://www.journals.cambridge.org/abstract{\_}S0305004100023793` doi: 10.1017/S0305004100023793

Blackadar, A. K., & Tennekes, H. (1968, nov). Asymptotic Similarity in Neutral Barotropic Planetary Boundary Layers. *J. Atmos. Sci.*, *25*, 1015–1020. doi: 10.1175/1520-0469(1968)025⟨1015:ASINBP⟩2.0.CO;2

Businger, J., Izumi, Y., Bradley, E., & Wyngaard, J. C. (1971). Flux-Profile Relationships in the Atmospheric Surface Layer. *J. Atmos. Sci.*, *28*, 9.

Chalikov, D. (1995, jun). *The Parameterization of the Wave Boundary Layer* (Vol. 25; Tech. Rep. No. 6). Retrieved from `http://journals.ametsoc.org/jpo/article-pdf/25/6/1333/4424635/1520-0485` doi: 10.1175/1520-0485(1995)025⟨1333:TPOTWB⟩2.0.CO;2

Chalikov, D., & Rainchik, S. (2011, jan). Coupled Numerical Modelling of Wind and Waves and the Theory of the Wave Boundary Layer. *Boundary-Layer Meteorol.*, *138*(1), 1–41. Retrieved from `http://link.springer.com/10.1007/s10546-010-9543-7` doi: 10.1007/s10546-010-9543-7

Chalikov, D. V. (1978). The Numerical Simulation of Wind-Wave Interaction. *J. Fluid Mech.*, *87*(3), 561–582. doi: https://doi.org/10.1017/S0022112078001767

Chalikov, D. V., & Makin, V. K. (1991, jul). Models of the wave boundary layer. *Boundary-Layer Meteorol.*, *56*(1-2), 83–99. Retrieved from `https://link.springer.com/article/10.1007/BF00119963` doi: 10.1007/BF00119963

Charnock, H. (1955). Wind Stress on a Water Surface. *Q. J. R. Meteorol. Soc.*, *81*(350), 1.

Cifuentes-Lorenzen, A., Edson, J. B., & Zappa, C. J. (2018, dec). Air-Sea Interaction in the Southern Ocean: Exploring the Height of the Wave Boundary Layer at the Air-Sea Interface. *Boundary-Layer Meteorol.*, *169*(3), 461–482. doi: 10.1007/s10546-018-0376-0

Donelan, M. A., Haus, B. K., Reul, N., Plant, W. J., Stiassnie, M., Graber, H. C., ... Saltzman, E. S. (2004). On the Limiting Aerodynamic Roughness of the Ocean in Very Strong Winds. *Geophys. Res. Lett.*, *31*(18), 5. doi: 10.1029/2004gl019460

Edson, J., Crawford, T., Crescenti, J., Farrar, T., Frew, N., Gerbi, G., ... Zappa, C. (2007, mar). The coupled boundary layers and air-sea transfer experiment in low winds. *Bull. Am. Meteorol. Soc.*, *88*(3), 341–356. Retrieved from `http://journals.ametsoc.org/bams/article-pdf/88/3/341/3736636/bams-88-3-341.pdf` doi: 10.1175/BAMS-88-3-341

Edson, J., Zappa, C., Ware, J., McGillis, W., & Hare, J. (2004). Scalar Flux Profile Relationships over the Open Ocean. *J. Geophys. Res.*, *109*(C08S09). doi: 10.1029/2003JC001960

Edson, J. B., & Fairall, C. W. (1998, jul). Similarity Relationships in the Marine Atmospheric Surface Layer for Terms in the TKE and Scalar Variance Budgets. *J. Atmos. Sci.*, *55*(13), 2311–2328. Retrieved from `http://journals.ametsoc.org/doi/abs/10.1175/1520-0469{\%}281998{\%}29055{\%}3C2311{\%}3ASRITMA{\%}3E2.0.CO{\%}3B2` doi: 10.1175/1520-0469(1998)055⟨2311:SRITMA⟩2.0.CO;2

Edson, J. B., Hinton, A. A., Prada, K. E., Hare, J. E., Fairall, C. W., Edson, J. B., ... Fairall, C. W. (1998, apr). Direct Covariance Flux Estimates from Mobile Platforms at Sea*. *J. Atmos. Ocean. Technol.*, *15*(2), 547–562. Retrieved from `http://journals.ametsoc.org/doi/abs/10.1175/1520-0426{\%}281998{\%}29015{\%}3C0547{\%}3ADCFEFM{\%}3E2.0.CO{\%}3B2` doi: 10.1175/1520-0426(1998)015⟨0547:DCFEFM⟩2.0.CO;2

Edson, J. B., Jampana, V., Weller, R. A., Bigorre, S. P., Plueddemann, A. J., Fairall, C. W., ... Hersbach, H. (2013). On the Exchange of Momentum over the Open Ocean. *J. Phys. Oceanogr.*, *43*(8), 22. doi: 10.1175/jpo-d-12-0173.1

Fairall, C. W., Bradley, E. F., Hare, J. E., Grachev, A. A., & Edson, J. B. (2003, feb). Bulk Parameterization of Air-Sea Fluxes: Updates and Verification for the COARE Algorithm. *http://dx.doi.org/10.1175/1520-0442(2003)016<0571:BPOASF>2.0.CO;2*. doi: 10.1175/1520-0442(2003)016⟨0571:BPOASF⟩2.0.CO;2

Fairall, C. W., Bradley, E. F., Rogers, D. P., Edson, J. B., & Young, G. S. (1996, feb). Bulk parameterization of air-sea fluxes for Tropical Ocean-Global Atmosphere Coupled-Ocean Atmosphere Response Experiment. *J. Geophys. Res. Ocean.*, *101*(C2), 3747–3764. Retrieved from `http://doi.wiley.com/10.1029/95JC03205` doi: 10.1029/95JC03205

Fang, P., Zhao, B., Zeng, Z., Yu, H., Lei, X., & Tan, J. (2018, jul). Effects of Wind Direction on Variations in Friction Velocity With Wind Speed Under Conditions of Strong Onshore Wind. *J. Geophys. Res. Atmos.*, *123*(14), 7340–7353. Retrieved from `http://doi.wiley.com/10.1029/2017JD028010` doi: 10.1029/2017JD028010

Fisher, F. H., & Spiess, F. N. (1963, oct). Flip-Floating Instrument Platform. *J. Acoust. Soc. Am.*, *35*(10), 1633–1644. Retrieved from `http://asa.scitation.org/doi/10.1121/1.1918772` doi: 10.1121/1.1918772

French, J. R., Drennan, W. M., Zhang, J. a., & Black, P. G. (2007, apr). Turbulent Fluxes in the Hurricane Boundary Layer. Part I: Momentum Flux. *J. Atmos. Sci.*, *64*(4), 1089–1102. Retrieved from `http://journals.ametsoc.org/doi/abs/10.1175/JAS3887.1` doi: 10.1175/JAS3887.1

Gentemann, C. L., Scott, J. P., Mazzini, P. L., Pianca, C., Akella, S., Minnett, P. J., ... Cohen, N. (2020, jan). Saildrone: adaptively sampling the marine environment. *Bull. Am. Meteorol. Soc.*. doi: 10.1175/bams-d-19-0015.1

Grachev, A. A., & Fairall, C. W. (2001, jul). Upward Momentum Transfer in the Marine Boundary Layer. *J. Phys. Oceanogr.*, *31*(7), 1698–1711. Retrieved from `http://journals.ametsoc.org/doi/abs/10.1175/1520-0485{\%}282001{\%}29031{\%}3C1698{\%}3AUMTITM{\%}3E2.0.CO{\%}3B2` doi: 10.1175/1520-0485(2001)031⟨1698:UMTITM⟩2.0.CO;2

Grachev, A. A., Fairall, C. W., Hare, J. E., Edson, J. B., & Miller, S. D. (2003, nov). Wind Stress Vector over Ocean Waves. *J. Phys. Oceanogr.*, *33*(11), 2408–2429. Retrieved from `http://journals.ametsoc.org/doi/abs/10.1175/1520-0485{\%}282003{\%}29033{\%}3C2408{\%}3AWSVOOW{\%}3E2`

.0.CO{\%}3B2 doi: 10.1175/1520-0485(2003)033⟨2408:WSVOOW⟩2.0.CO;2
Grare, L., Lenain, L., & Melville, W. K. (2013, oct). Wave-Coherent Airflow and Critical Layers over Ocean Waves. *J. Phys. Oceanogr.*, *43*(10), 2156–2172. Retrieved from http://journals.ametsoc.org/doi/abs/10.1175/JPO-D-13-056.1 doi: 10.1175/JPO-D-13-056.1
Högström, U., Rutgersson, A., Sahlée, E., Smedman, A.-S., Hristov, T. S., Drennan, W. M., & Kahma, K. K. (2013, apr). Air-Sea Interaction Features in the Baltic Sea and at a Pacific Trade-Wind Site: An Inter-comparison Study. *Q. J. R. Meteorol. Soc. Meteorol.*, *147*(1), 139–163. Retrieved from http://link.springer.com/10.1007/s10546-012-9776-8 doi: 10.1007/s10546-012-9776-8
Hogstrom, U., Sahlee, E., Drennan, W. M., Kahma, K. K., Johansson, C., Petersson, H., ... Johansson, M. (2008). Momentum Fluxes and Wind Gradients in the Marine Boundary Layer — a Multi-Platform Study. *Boreal Environ. Res.*(13), 27.
Högström, U., Sahlée, E., Smedman, A.-S., Rutgersson, A., Nilsson, E., Kahma, K. K., & Drennan, W. M. (2015). Surface Stress over the Ocean in Swell-Dominated Conditions during Moderate Winds. *J. Atmos. Sci.*, *72*, 18. Retrieved from http://journals.ametsoc.org/doi/pdf/10.1175/JAS-D-15-0139.1 doi: 10.1175/JAS-D-15-0139.1
Högström, U., Sahlée, E., Smedman, A.-S., Rutgersson, A., Nilsson, E., Kahma, K. K., & Drennan, W. M. (2018, aug). The Transition from Downward to Upward Air-Sea Momentum Flux in Swell-Dominated Light Wind Conditions. *J. Atmos. Sci.*, *75*(8), 2579–2588. Retrieved from http://journals.ametsoc.org/doi/10.1175/JAS-D-17-0334.1 doi: 10.1175/JAS-D-17-0334.1
Hristov, T., Friehe, C., & Miller, S. (1998). Wave-Coherent Fields in Air Flow over Ocean Waves: Identification of Cooperative Behavior Buried in Turbulence. *Phys. Rev. Lett.*, *81*(23), 5245–5248. doi: 10.1103/PhysRevLett.81.5245
Hristov, T., & Ruiz-Plancarte, J. (2014). Dynamic balances in a wavy boundary layer. *J. Phys. Oceanogr.*, *44*(12), 3185–3194. doi: 10.1175/JPO-D-13-0209.1
Janssen, P. A. E. M. (1989, jun). Wave-Induced Stress and the Drag of Air Flow over Sea Waves. *J. Phys. Oceanogr.*, *19*(6), 745–754. Retrieved from http://journals.ametsoc.org/doi/abs/10.1175/1520-0485(1989)019{\%}3C0745:WISATD{\%}3E2.0.CO;2 doi: 10.1175/1520-0485(1989)019⟨0745:WISATD⟩2.0.CO;2
Jeong, D., Haus, B. K., & Donelan, M. A. (2012, sep). Enthalpy Transfer across the Air-Water Interface in High Winds Including Spray. *J. Atmos. Sci.*, *69*(9), 2733–2748. doi: 10.1175/JAS-D-11-0260.1
Kak, S. C. (1970). The Discrete Hilbert Transform. *Proc. IEEE*, *58*(4), 585–586. doi: 10.1109/PROC.1970.7696
Katz, J., & Zhu, P. (2017, sep). Evaluation of surface layer flux parameterizations using in-situ observations. *Atmos. Res.*, *194*, 150–163. Retrieved from https://www.sciencedirect.com/science/article/pii/S0169809516307165 doi: 10.1016/J.ATMOSRES.2017.04.025
Kitaigorodskii, S., & Volkov, Y. A. (1965). On the Roughness Parameter of the Sea Surface and the Calculation of Momentum Rlux in the Near-Water Layer of the Atmosphere. *Izv. Atmos. Ocean. Phys*, *1*, 973—-988.
Kolmogorov, A. (1941a). Dissipation of Energy in Locally Isotropic Turbulence. *Comptes Rendus l'Acadamie des Sci. l'U.R.S.S.*, *32*, 16.
Kolmogorov, A. (1941b). The Local Structure of Turbulence in Incompressible Viscous Fluid for Very Large Reynolds Numbers. *Dokl. Akad. Nauk SSSR.* Retrieved from http://homepages.see.leeds.ac.uk/{~}eeaol/p/kolmogorov41.pdf
Kraus, E., & Businger, J. (1994). *Atmosphere-Ocean Interaction.* New York: Oxford

University Press.
Large, W., & Pond, S. (1981). Open Ocean Momentum Flux Measurements in Moderate to Strong Winds. *J. Phys. Oceanogr.*, *11*, 13.
Large, W. G., & Pond, S. (1982, may). Sensible and Latent Heat Flux Measurements over the Ocean. *J. Phys. Oceanogr.*, *12*(5), 464–482. doi: 10.1175/1520-0485(1982)012⟨0464:SALHFM⟩2.0.CO;2
Li, Q., Bou-Zeid, E., Vercauteren, N., & Parlange, M. (2018, jun). Signatures of Air-Wave Interactions Over a Large Lake. *Boundary-Layer Meteorol.*, *167*(3), 445–468. Retrieved from `http://link.springer.com/10.1007/s10546-017-0329-z` doi: 10.1007/s10546-017-0329-z
Mahrt, L., Miller, S., Hristov, T., & Edson, J. (2018, jul). On Estimating The Surface wind stress over the sea. *J. Phys. Oceanogr.*, *48*(7), 1533–1541. Retrieved from `www.ametsoc.org/PUBSReuseLicenses` doi: 10.1175/JPO-D-17-0267.1
Martins, L. G. N., Miller, S. D., & Acevedo, O. C. (2017, apr). Using Empirical Mode Decomposition to Filter Out Non-turbulent Contributions to Air-Sea Fluxes. *Boundary-Layer Meteorol.*, *163*(1), 123–141. doi: 10.1007/s10546-016-0215-0
Miller, S. D., Friehe, C. A., Hristov, T. S., Edson, J. B., & Wetzel, S. (1999). Wind and Turbulence Profiles in the Surface Layer Over Ocean Waves. In S. G. Sajjadi, N. H. Thomas, & J. C. R. Hunt (Eds.), *Wind. couplings perspect. prospect.* (1st ed., chap. 10). New York: Oxford University Press.
Miller, S. D., Hristov, T. S., Edson, J. B., & Friehe, C. A. (2008). Platform Motion Effects on Measurements of Turbulence and Air-Sea Exchange over the Open Ocean. *J. Atmos. Ocean. Technol.*, *25*, 1683–1694. Retrieved from `https://journals.ametsoc.org/doi/pdf/10.1175/2008JTECHO547.1` doi: 10.1175/2008JTECHO547.1
Ortiz-Suslow, D. G., Haus, B. K., Williams, N. J., Graber, H. C., & MacMahan, J. H. (2018, dec). Observations of Air-Sea Momentum Flux Variability Across the Inner Shelf. *J. Geophys. Res. Ocean.*, *123*(12), 2018JC014348. Retrieved from `https://onlinelibrary.wiley.com/doi/abs/10.1029/2018JC014348` doi: 10.1029/2018JC014348
Ortiz-Suslow, D. G., Haus, B. K., Williams, N. J., Laxague, N. J. M., Reniers, A. J. H. M., & Graber, H. C. (2015, feb). The Spatial-Temporal Variability of Air-Sea Momentum Fluxes Observed at a Tidal Inlet. *J. Geophys. Res. Ocean.*, *120*(2), 660–676. Retrieved from `http://doi.wiley.com/10.1002/2014JC010412` doi: 10.1002/2014JC010412
Ortiz-Suslow, D. G., Kalogiros, J., Yamaguchi, R., Alappattu, D., Franklin, K., Wauer, B., & Wang, Q. (2019). *The Data Processing and Quality Control of the Marine Atmospheric Boundary Layer Measurement Systems Deployed by the Naval Postgraduate School during the CASPER-West Field Campaign* (Tech. Rep.). Monterey, CA: Naval Postgraduate School. Retrieved from `https://calhoun.nps.edu/handle/10945/61638` doi: NPS-MR-19-001
Ortiz-Suslow, D. G., & Wang, Q. (2019, dec). An Evaluation of Kolmogorov's -5/3 Power Law Observed within the Turbulent Airflow above the Ocean. *Geophys. Res. Lett.*, *46*, 2019GL085083. Retrieved from `https://onlinelibrary.wiley.com/doi/abs/10.1029/2019GL085083` doi: 10.1029/2019GL085083
Potter, H. (2015, feb). Swell and the Drag Coefficient. *Ocean Dyn.*, *65*(3), 375–384. Retrieved from `http://link.springer.com/10.1007/s10236-015-0811-4` doi: 10.1007/s10236-015-0811-4
Potter, H., Graber, H. C., Williams, N. J., Collins, C. O., Ramos, R. J., & Drennan, W. M. (2015, jan). In situ Measurements of Momentum Fluxes in Typhoons. *J. Atmos. Sci.*, *72*(1), 104–118. doi: 10.1175/JAS-D-14-0025.1
Powell, M. D., Vickery, P. J., & Reinhold, T. A. (2003, mar). Reduced Drag Coefficient for High Wind Speeds in Tropical Cyclones. *Nature*, *422*(6929), 279–83. doi: 10.1038/nature01481

Rieder, K. F., & Smith, J. A. (1994). Observed Directional Characteristics of the Wind, Wind stress, and Surface waves on the Open Ocean. *J. Geophys. Res.*, *99*, 7.

Rogers, R., & Yau, M. (1989). *A Short Course in Cloud Physics* (3rd ed.). Oxford: Pergamon Press. Retrieved from `https://books.google.com/books?hl=en{\&}lr={\&}id=ClKbCgAAQBAJ{\&}oi=fnd{\&}pg=PP1{\&}dq=A+Short+Course+in+Cloud+Physics{\&}ots=EmFRBL1SHO{\&}sig=HaUgEo9wKwBfpDp28unEDbQnuGU{\#}v=onepage{\&}q=AShortCourseinCloudPhysics{\&}f=false`

Scully, M. E., Trowbridge, J. H., Sherwood, C. R., Jones, K. R., & Traykovski, P. (2018, apr). Direct Measurements of Mean Reynolds Stress and Ripple Roughness in the Presence of Energetic Forcing by Surface Waves. *J. Geophys. Res. Ocean.*, *123*(4), 2494–2512. Retrieved from `http://doi.wiley.com/10.1002/2017JC013252` doi: 10.1002/2017JC013252

Shabani, B., Nielsen, P., & Baldock, T. (2014, may). Direct Measurements of Wind Stress over the Surf Zone. *J. Geophys. Res. Ocean.*, *119*(5), 2949–2973. Retrieved from `http://doi.wiley.com/10.1002/2013JC009585` doi: 10.1002/2013JC009585

Smedman, A., Högström, U., Bergström, H., Rutgersson, A., Kahma, K. K., & Pettersson, H. (1999). A Case Study of Air-Sea Interaction during Swell Conditions. *J. Geophys. Res.*, *104*(C11), 25833. doi: 10.1029/1999jc900213

Smith, S. D. (1980). Wind Stress and Heat Flux over the Ocean in Gale Force Winds. *J. Phys. Oceanogr.*, *10*, 18.

Smith, S. D. (1988). Coefficients for Sea Surface Wind Stress, Heat Flux, and Wind Profiles as a Function of Wind Speed and Temperature. *J. Geophys. Res.*, *93*(C12), 15467. doi: 10.1029/JC093iC12p15467

Smith, S. D., & Banke, E. G. (1975). Variation of the Sea Surface Drag Coefficient with Wind Speed. *Q. J. R. Meteorol. Soc.*, *101*, 8.

Sullivan, P. P., Banner, M. L., Morison, R. P., & Peirson, W. L. (2018, jan). Turbulent flow over steep steady and unsteady waves under strong wind forcing. *J. Phys. Oceanogr.*, *48*(1), 3–27. Retrieved from `www.ametsoc.org/PUBSReuseLicenses` doi: 10.1175/JPO-D-17-0118.1

Tennekes, H. (1973). The Logarithmic Wind Profile. *J. Atmos. Sci.*, *30*, 234–238.

Tennekes, H., & Lumley, J. (1972). *A First Course inTturbulence.* Cambridge, Massachusetts: MIT Press.

Thomson, J., Girton, J. B., Jha, R., & Trapani, A. (2018, feb). Measurements of Directional Wave Spectra and Wind Stress from a Wave Glider Autonomous Surface Vehicle. *J. Atmos. Ocean. Technol.*, *35*(2), 347–363. Retrieved from `http://journals.ametsoc.org/doi/10.1175/JTECH-D-17-0091.1` doi: 10.1175/JTECH-D-17-0091.1

Wang, Q., Alappattu, D. P., Billingsley, S., Blomquist, B., Burkholder, R. J., Christman, A. J., … Yardim, C. (2018, nov). CASPER: Coupled Air-Sea Processes and Electromagnetic (EM) ducting Research. *Bull. Am. Meteorol. Soc.*, *99(7)*, 1449–1471. Retrieved from `http://journals.ametsoc.org/doi/10.1175/BAMS-D-16-0046.1` doi: 10.1175/BAMS-D-16-0046.1

Wetzel, S. (1996). *An Investigation of Wave-Induced Momentum Flux Through Phase Averging of Ocean Ocean Wind and Wave Fields* (Unpublished doctoral dissertation). MIT/WHOI.

Wilczak, J. M., Oncley, S. P., & Stage, S. A. (2000). Sonic Anemometer Tilt Correction Algorithms. *Boundary-Layer Meteorol.*, *99*, 24.

Wu, J. (1982). Wind-stress Coefficients over Sea Surface from Breeze to Hurricane. *J. Geophys. Res.*, *87*(C12), 9704. Retrieved from `http://doi.wiley.com/10.1029/JC087iC12p09704` doi: 10.1029/JC087iC12p09704

Wyngaard, J. C. (1990, mar). Scalar fluxes in the planetary boundary layer-Theory, modeling, and measurement. *Boundary-Layer Meteorol.*, *50*(1-4), 49–75. Retrieved from http://link.springer.com/10.1007/BF00120518 doi: 10.1007/BF00120518

Wyngaard, J. C. (2010). *Turbulence in the Atmosphere* (1st ed.). Cambridge: Cambridge University Press.

Yamaguchi, R. T., Wang, Q., & Kalogiros, J. A. (2020). Wave Glider Measurements of Turbulent Fluxes and Bulk Meteorological Quantities in the Wave Boundary Layer. In *100th am. meteorol. soc. annu. meet.* Boston.

Yang, D., & Shen, L. (2017). Direct numerical simulation of scalar transport in turbulent flows over progressive surface waves. *J. Fluid Mech*, *819*, 58–103. doi: 10.1017/jfm.2017.164

Yelland, M., & Taylor, P. K. (1996). Wind Stress Measurements from the Open Ocean. *J. Phys. Oceanogr.*, *26*, 18.

Zhang, F. W., Drennan, W. M., Haus, B. K., & Graber, H. C. (2009). On Wind-Wave-Current Interactions during the Shoaling Waves Experiment. *J. Geophys. Res.*, *114*(C1), 12. doi: 10.1029/2008jc004998

Zhao, Z.-K., Liu, C.-X., Li, Q., Dai, G.-F., Song, Q.-T., & Lv, W.-H. (2015, jan). Typhoon Air-Sea Drag Coefficient in Coastal Regions. *J. Geophys. Res. Ocean.*, n/a–n/a. Retrieved from http://doi.wiley.com/10.1002/2014JC010283 doi: 10.1002/2014JC010283